


First-principles analysis of intercalated Pb structures under buffer-layer graphene on SiC(0001): Pb(111)-, plumbene-, and amorphous-like Pb layers

Yong Han ^{1,2,*}, Marek Kolmer ¹, James W. Evans ^{1,2} and Michael C. Tringides ^{1,2}

¹Ames National Laboratory, U. S. Department of Energy, Ames, Iowa 50011, USA

²Department of Physics and Astronomy, Iowa State University, Ames, Iowa 50011, USA

 (Received 30 November 2023; revised 5 February 2024; accepted 4 March 2024; published 4 April 2024)

The electronic properties of two-dimensional (2D) material systems strongly depend on their atomic arrangement, so validating the structure of an experimentally fabricated 2D system is an important task for researchers. First-principles density-functional theory (DFT) is used to analyze about 100 configurations of Pb intercalated under buffer-layer graphene on SiC(0001). These configurations are constructed by using seven different types of supercells corresponding to varying strain. By comparing the chemical potentials of the intercalated Pb structures, we find that the thermodynamically most preferred intercalated Pb configurations appear under the low-strained buffer-layer graphene. We also find that plentiful structures with the lowest chemical potentials are amorphous-like Pb monolayers. These are almost energetically degenerate with various Pb(111)-like monolayers having slightly higher chemical potentials. Our DFT results also indicate that intercalated plumbene-like monolayers under the high-strained buffer-layer graphene generally have higher chemical potentials. However, intercalated plumbene-like monolayers under a low-strained buffer-layer graphene do also exist with significantly lower chemical potentials relative to the structures under the high-strained buffer-layer graphene, despite some distortions in their structures. These results are consistent with previously available experimental results and suggest further studies on this unique system to promote the synthesis of phases with the anticipated properties, which are attractive for applications.

DOI: [10.1103/PhysRevMaterials.8.044002](https://doi.org/10.1103/PhysRevMaterials.8.044002)

I. INTRODUCTION

Growing high-quality two-dimensional (2D) heterostructures with novel electronic properties often involves intercalation of heteroatoms within interlayer spaces of layered materials [1–6]. Recent experimental studies [7–16] for Pb intercalation under single-layer graphene (SLG) or under buffer-layer graphene supported on Si-terminated SiC(0001) substrates have been performed. Here, the buffer-layer graphene is epitaxially bound to the Si-terminated SiC(0001) surface and is often called zero-layer graphene (ZLG) in the literature, while SLG refers specifically to a single graphene on top of ZLG. There are at least two reasons that the Pb-intercalated graphene-SiC system has been intensively studied. One reason is the interesting behavior theoretically predicted in this system, e.g., electronic properties of epitaxial graphene above SiC substrate can be manipulated by tuning intercalation conditions, such as location of intercalated Pb, coverage of Pb, and thickness of graphene layer [17]. Another reason is that Pb is well known to exhibit superconductivity, even down to 2D ultrathin films [18,19], as a heavy element with strong spin-orbit coupling [20,21]. Thus, it is natural to reexamine the superconductivity of Pb when it is an intercalant within a gallery of a layered material. Recently, a 2D Pb monolayer intercalated under ZLG on a Si-terminated SiC(0001) substrate has been theoretically demonstrated to be

a potentially attractive platform for spintronics applications [22,14].

Previous experiments for Pb deposition on graphene supported on a SiC(0001) substrate [7–13] have shown that intercalation of Pb can be initiated at around 450 °C. During annealing of the system, the most preferred position of intercalated Pb is the gallery between ZLG and the Si-terminating layer (STL) of SiC(0001) substrate. Pb atoms exhibit high mobility on top of graphene [23] and it has been suggested that Pb can easily reach the surface inhomogeneities, such as domain boundaries and step edges of graphene, and then move below [8–10]. Measurements from scanning tunneling microscopy (STM) suggest that the intercalated Pb forms a single-atom-thick layer, which can persist for several months even under ambient conditions [7]. This indicates a relatively high thermal stability of the intercalated Pb monolayer. In contrast, a recent experimental analysis supports the formation of Pb multilayers at the interface [13].

To assess thermodynamics and kinetics of Pb intercalation under SLG versus under ZLG, we have recently performed our density-functional theory (DFT) analysis [24], revealing a dependence of the most favored location on coverage and subsurface position of intercalated Pb, as well as elucidating the complexity of Pb intercalation pathways. For simplicity, this analysis assumed that the intercalated Pb monolayer has a Pb(111) structure. In contrast to this simplified picture, we have also found a family of more complex, thermodynamically preferred Pb-intercalated phases with a high degree of energetic degeneracy [16]. Specifically, in this work, we

*y27h@ameslab.gov

perform a comprehensive structural analysis for about 100 configurations of Pb-intercalated ZLG-SiC(0001) system at low Pb coverages. Clarification of intercalated structures is extremely important because electronic properties of a 2D material can strongly depend on its structure or phase [1–6]. As an example, a recent finding is that structural disorder in an amorphized hydrogenated α -Sn(111) monolayer can induce electronic order of topology in an otherwise topologically trivial crystal [25]. This indicates that verifying the amorphization of a 2D monolayer for specific synthesis conditions is prerequisite for further investigation of its relevant electronic properties, as will be analyzed in detail for the structures of intercalated Pb layers in this work.

On the other hand, plumbene has been the recent focus of many studies [26–42,13] as have its cousins silicene, germanene, stanene, phosphorene, bismuthene, tellurene, etc. [28,32,38,40] with graphene-like honeycomb lattices. DFT has predicted that freestanding plumbene has a large band gap of about 0.4 eV [31]. By electron doping, plumbene can become a topological insulator still with a large gap of about 0.2 eV, where the nontrivial state is very robust under external strain [31]. The large band gaps and stable edge states in plumbene make it an ideal candidate for realizing the quantum spin Hall effect and designing spintronic devices at room temperature. DFT has also predicted that bilayer plumbene and decorated plumbene can become giant-gap quantum spin Hall insulators [30,34]. In addition, molecular dynamics simulations of the mechanical properties of plumbene reveal particularly high yield strength and tensile strength amongst other features [33]. Furthermore, DFT results show that plumbene exhibits a significantly higher hydrogen gravimetric density of 6.74 wt. % than other 2D-like materials, such as silicene, germanene, h-BN, MoS₂, black phosphorene, holey-C₂N, etc., and thus is also considered as an ideal hydrogen storage material [42]. Experimentally, however, growth studies of plumbene are limited, especially on graphitic substrates. There has been evidence that plumbene can be epitaxially grown on a Pd-Pb alloy surface [35] and forms on an Fe monolayer on Ir(111) substrate [37]. In recent experiments involving Pb intercalation, two stacked plumbene honeycomb lattices were observed under graphene on SiC(0001) substrate [13]. In this work, partly motivated by this recent experimental report, we will examine the thermodynamic favorability of plumbene formation by relaxing multiple selected configurations for intercalated Pb under differently strained ZLG on SiC (0001).

To understand the structures and electronic properties of the intercalated Pb layer under the buffer-layer graphene, extensive experimental work has been carried out during the last few years by using different experimental techniques including surface diffraction, STM/STS (scanning tunneling microscopy/spectroscopy), and angle-resolved photoemission spectroscopy (ARPES) with the theoretical analyses from DFT calculations [7–16,24]. Despite the multiple studies, major open questions remain and need to be resolved. This ongoing effort to clarify the structure of the intercalated Pb layer has motivated partially the present work by exploring a much wider range of possible phases which differ in periodicity, Pb coverage, and local ordering, but have similar thermodynamic stabilities.

In our earlier study [16], we have shown that Pb phases which differ in Pb crystallinity and coverage can have very close chemical potentials. This implies that such intercalated Pb phases can coexist under the experimental conditions. Despite the large size of the Pb atom, intercalation occurs at the relatively low temperature of 450 °C with both deintercalation and eventual desorption proceeding at only 200 °C higher, suggesting facile exchange between the top and below graphene planes. This possibility can partially explain why the experimentally observed diffraction spots for Pb superstructures with a 10×10 periodicity (based on the graphene primitive cell) have very low intensity, over a range of growth conditions used to avoid kinetic limitations and low annealing temperatures. The low intensity of the 10×10 spot most likely occurs for additional reasons, since it is only observed at a handful of electron energies in diffraction, and this is usually a sign that electronic effects relating the intercalated layer and graphene or Pb(111) islands on top might be relevant. Further support of the complexity of the intercalated Pb heterostructure is seen from ARPES spectra, which are of the highest quality despite the diffraction spots being very weak. The measured ARPES spectra are characterized by strong Pb bands close to the Fermi level, and several replica Dirac cones are present with wave vectors paradoxically related to both SiC(0001) and graphene lattices [15]. This suggests the existence of an electronically coherent heterostructure and that the graphene electrons experience a new term in their Hamiltonian. In addition, Pb intercalation kinetics has been theoretically analyzed [24]. For an intercalated Pb monolayer forming around a graphene defect including step edges, facile Pb mass transport can be initiated by Pb vacancy-mediated diffusion for continued growth of the intercalated monolayer. This is also consistent with the experimentally observed high exchange rate of Pb atoms between planes atop and below graphene.

Another major open question is the thickness of the intercalated Pb layer. Based on STM images and spot-profile analysis of low-energy electron-diffraction (LEED) patterns showing two symmetric spots around the [1100] direction, it was deduced that intercalated plumbene consists of two stacked Pb monolayers rotated in opposite directions [13]. However, standing-wave x-ray analysis of the diffraction spots has shown that only one Pb monolayer forms but with the interlayer spacing changing from 0.24 nm for the pristine graphene (before Pb intercalation) to 0.64 nm [15]. As also suggested [15], the intercalated Pb is possibly another manifestation of the outstanding prediction of a Devil's Staircase in surface overlayers, and thus is it possible that both phases can form under different conditions. In this work, we have performed extensive DFT calculations to address this question as well as the broader issue about the thermodynamic stability of intercalated plumbene monolayers. Our results support the picture that monolayer plumbene can form but its lattice becomes distorted in a locally metastable equilibrium configuration.

This paper is organized as follows. Section II describes the DFT methodology used in this study. In Sec. III, we analyze geometric parameters of freestanding Pb(111) monolayer, Pb(111) bilayer, and plumbene from our DFT calculations. In Sec. IV and Sec. V, we discuss and compare Pb

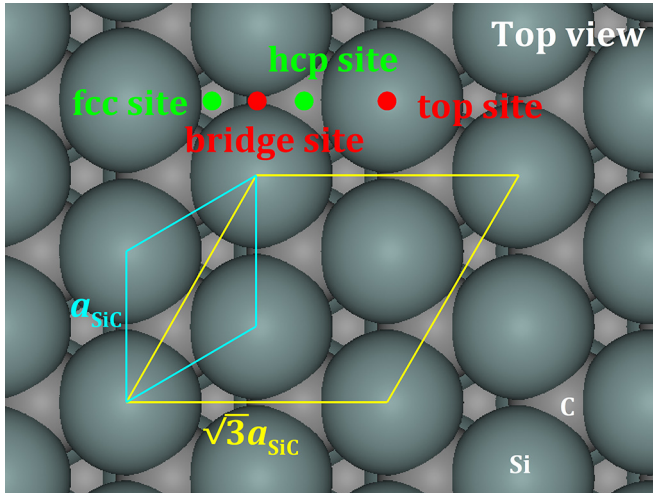


FIG. 1. Top view of Si-terminated SiC(0001). The primitive cell (cyan rhombus) and $\sqrt{3}a_{\text{SiC}} \times \sqrt{3}a_{\text{SiC}}$ unit cell (yellow rhombus) of SiC(0001) surface. The four high-symmetry sites (fcc, hcp, top, and bridge sites) on the surface are indicated.

intercalation under buffer-layer graphene (ZLG) on SiC(0001) from analysis with seven different supercells. In Sec. VI, we provide a summary. Appendix A provides the information on lattice mismatch and strain in graphene, Pb(111), and plumbene relative to SiC(0001). Our DFT data for 104 analyzed configurations are listed in Appendix B with Supplemental Material [43].

II. DFT METHODOLOGY

For all DFT calculations in this work, we use the VASP code [44] with the Projector augmented wave potentials from the VASP group [45] and the optB88-vdW functional [46] with the van der Waals (vdW) interactions from an optimization of Becke's exchange-energy functional in 1988. For the periodic slab of ZLG plus Si-terminated SiC(0001) system, we use a rhombic supercell with the lateral size of $ma_G^* \times ma_G^*$ matching $n\sqrt{3}a_{\text{SiC}} \times n\sqrt{3}a_{\text{SiC}}$ [denoted as $(m \times m)G/(n \times n)Si$ below for conciseness], where a_{SiC} is the lattice constant of 6H-SiC crystal and the strained ZLG lattice constant $a_G^* = n\sqrt{3}a_{\text{SiC}}/m$, according to the experimental observations that there is an angle of 30° between primitive cells of ZLG and SiC(0001) [47–49]. See Fig. 1 for the primitive cell and $\sqrt{3}a_{\text{SiC}} \times \sqrt{3}a_{\text{SiC}}$ unit cell of the SiC(0001) surface. The number of Si atoms in STL is given by $N = 3n^2$ because three such $n \times n$ SiC(0001) unit cells fit the $m \times m$ graphene unit cell approximately.

For a rhombic supercell $(m \times m)G/(n \times n)Si$ without intercalated Pb, the corresponding ZLG-SiC lattice mismatch is given by a lateral strain:

$$\varepsilon_G = \frac{n\sqrt{3}a_{\text{SiC}} - ma_G}{ma_G} \times 100\%, \quad (1)$$

where a_G is the equilibrium lattice constant of freestanding graphene. A tensile (compressive) strain $\varepsilon_G > 0$ ($\varepsilon_G < 0$) means that ZLG is laterally stretched (compressed) relative to the unstrained freestanding graphene. In order to reduce

the amount of the computation and based upon experimental observations, one should choose the smallest possible supercell sizes (specified by the positive integers m and n) with the smallest possible magnitude of the corresponding ε_G value. Considering this requirement, we select seven types of supercells: $(2 \times 2)G/(1 \times 1)Si$, $(4 \times 4)G/(2 \times 2)Si$, $(6 \times 6)G/(3 \times 3)Si$, $(10 \times 10)G/(5 \times 5)Si$, $(13 \times 13)G/(6 \times 6)Si$, $(20 \times 20)G/(9 \times 9)Si$, and $(26 \times 26)G/(12 \times 12)Si$. As listed in column 2 in Table I in Appendix A, the first four smallest supercells correspond to a relatively larger tensile strain $\varepsilon_G \approx +8.8\%$, the fifth and the seventh correspond to a tiny tensile strain $\varepsilon_G \approx +0.4\%$, and the sixth corresponds to a small compressive strain $\varepsilon_G \approx -2.1\%$, when we take our DFT values $a_{\text{SiC}} = 3.09545 \text{ \AA}$ and $a_G = 2.464 \text{ \AA}$ [50]. The experimental observations show that one 13×13 graphene unit cell ($m = 13$) matches three 6×6 SiC(0001) unit cells ($n = 6$) [49]. This implies that the thermodynamically most preferred structures in experiments adopt the lowest strain $\varepsilon_G \approx +0.4\%$. In this work, we not only consider the supercells $(13 \times 13)G/(6 \times 6)Si$ and $(26 \times 26)G/(12 \times 12)Si$ with the lowest strain, but also consider the other four supercells with higher strain. The rationale is that graphene is expected to relax depending on the experimental conditions resulting in significant corrugation, and then the higher local strains are likely realized, where a minority fraction of higher-strain phases might be kinetically easier to form and randomly distributed within the majority low-strained phases [51,52].

In our calculations for Pb intercalation, we insert a Pb layer which can be a Pb(111) monolayer, a plumbene monolayer, or a Pb(111) bilayer with a supercell size $la_0^* \times la_0^*$ (shortened as $l \times l$ below), where the strained Pb layer lattice constant $a_0^* = n\sqrt{3}a_{\text{SiC}}/l$. For unstrained lattice parameter a_0 of these Pb layers, see the analysis in Sec. III. For an intercalated $l \times l$ Pb layer, the corresponding Pb-STL lattice mismatch is given by a lateral strain:

$$\varepsilon_{\text{Pb}} = \frac{n\sqrt{3}a_{\text{SiC}} - la_0}{la_0} \times 100\%, \quad (2)$$

where there is an angle of 30° between primitive cells of Pb(111) (or plumbene) and SiC(0001), i.e., we here assume that an intercalated Pb(111) layer has the same orientation as graphene [12]. A tensile (compressive) strain $\varepsilon_{\text{Pb}} > 0$ ($\varepsilon_{\text{Pb}} < 0$) indicates that the Pb layer is laterally stretched (compressed) relative to the unstrained freestanding Pb layer. In Appendix A, we list the relatively low ε_{Pb} values for given $l \times l$. In our calculations, we select the supercells of initially intercalated Pb layer by considering these low-strain values. In addition to the above, we also select other initial structures of interest, e.g., a Pb layer modified from an already fully relaxed configuration by removing or adding specific Pb atoms, a $l \times l_{\text{R30}}$ Pb layer, etc. Here, $l \times l_{\text{R30}}$ denotes a configuration with an angle of 30° between primitive cells of Pb(111) and graphene, i.e., an intercalated Pb(111) layer has the same orientation as SiC(0001) substrate. The experimental evidence supporting such a supercell of $l \times l_{\text{R30}}$ has been discussed recently [14].

In our slab calculations, the energy cutoff is set to be 550 eV. The force convergence tolerance is set to be less

TABLE I. Strains ε_G in graphene and ε_{Pb} in $l \times l$ Pb layers relative to SiC(0001) along the $\sqrt{3}a_{SiC} \times \sqrt{3}a_{SiC}$ unit cell for seven types of supercells, calculated from Eqs. (1) and (2), where the lattice constants are taken to be $a_{SiC} = 3.09545 \text{ \AA}$ for SiC(0001) substrate [51], $a_G = 2.464 \text{ \AA}$ for freestanding graphene [50], $a_0 = 3.290 \text{ \AA}$ for a Pb(111) monolayer, $a_0 = 3.519 \text{ \AA}$ for a Pb(111) bilayer, $a_0 = 3.546 \text{ \AA}$ for a bulk Pb(111) slab, and $a_0 = 4.904 \text{ \AA}$ for plumbene (see Sec. III).

Supercell	Graphene ε_G (%)	Pb layer $l \times l$	Pb(111) monolayer ε_{Pb} (%)	Pb(111) bilayer ε_{Pb} (%)	Bulk Pb(111) slab ε_{Pb} (%)	Plumbene ε_{Pb} (%)
$(2 \times 2)G/(1 \times 1)Si$	+8.8	1×1	+63.0	+52.4	+51.2	+9.3
		2×2	-18.5	-23.8	-24.4	-45.3
$(4 \times 4)G/(2 \times 2)Si$	+8.8	2×2	+63.0	+52.4	+51.2	+9.3
		3×3	+8.6	+1.6	+0.8	-27.1
		4×4	-18.5	-23.8	-24.4	-45.3
$(6 \times 6)G/(3 \times 3)Si$	+8.8	3×3	+63.0	+52.4	+51.2	+9.3
		4×4	+22.2	+14.3	+13.4	-18.0
		5×5	-2.2	-8.6	-9.3	-34.4
		6×6	-18.5	-23.8	-24.4	-45.3
$(10 \times 10)G/(5 \times 5)Si$	+8.8	5×5	+63.0	+52.4	+51.2	+9.3
		6×6	+35.8	+27.0	+26.0	-8.9
		7×7	+16.4	+8.8	+8.0	-21.9
		8×8	+1.9	-4.8	-5.5	-31.7
		9×9	-9.5	-15.4	-16.0	-39.3
		10×10	-18.5	-23.8	-24.4	-45.3
$(13 \times 13)G/(6 \times 6)Si$	+0.4	6×6	+63.0	+52.4	+51.2	+9.3
		7×7	+39.7	+30.6	+29.6	-6.3
		8×8	+22.2	+14.3	+13.4	-18.0
		9×9	+8.6	+1.6	+0.8	-27.1
		10×10	-2.2	-8.6	-9.3	-34.4
		11×11	-11.1	-16.9	-17.0	-40.4
$(20 \times 20)G/(9 \times 9)Si$	-2.1	12×12	-18.5	-23.8	-24.4%	-45.3
		9×9	+63.0	+52.4	+51.2	+9.3
		10×10	+46.7	+37.1	+36.1	-1.6
		11×11	+33.3	+24.7	+23.7	-10.5
		12×12	+22.2	+14.3	+13.4	-18.0
		13×13	+12.8	+5.5	+4.7	-24.3
		14×14	+4.8	-2.1	-2.8	-29.7
		15×15	-2.2	-8.6	-9.3	-34.4
		16×16	-8.3	-14.3	-15.0	-38.5
		17×17	-13.7	-19.3	-20.0	-42.1
		18×18	-18.5	-23.8	-24.4	-45.3
$(26 \times 26)G/(12 \times 12)Si$	+0.4	12×12	+63.0	+52.4	+51.2	+9.3
		13×13	+50.4	+40.6	+39.6	+0.9
		14×14	+39.7	+30.6	+29.6	-6.3
		15×15	+30.4	+21.9	+21.0	-12.5
		16×16	+22.2	+14.3	+13.4	-18.0
		17×17	+15.0	+7.5	+6.7	-22.8
		18×18	+8.6	+1.6	+0.8	-27.1
		19×19	+2.9	-3.8	-4.5	-31.0
		20×20	-2.2	-8.6	-9.3	-34.4
		21×21	-6.9	-12.9	-13.6	-37.5
22×22	-11.1	-16.9	-17.5	-40.4		
23×23	-15.0	-20.5	-21.1	-43.0		
24×24	-18.5	-23.8	-24.4	-45.3		

than 0.005 eV/\AA . Spin polarization and dipole corrections are always considered. Along the direction perpendicular to the slab surface, the vacuum thickness is taken to be not smaller than 2 nm. For smaller supercells: $(2 \times 2)G/(1 \times 1)Si$, $(4 \times 4)G/(2 \times 2)Si$, and $(6 \times 6)G/(3 \times 3)Si$, we fix the bottommost C-Si monolayer of three C-Si monolayers of the SiC substrate during the relaxation, as done previously [24]. The large supercell calculations are extremely demanding,

so we remove a C-Si monolayer from the SiC substrate and only fix the bottommost single-atom-thick C layer during the relaxation. In fact, the effect of reducing substrate thickness from three to two C-Si layers on the relaxed geometry is not significant [51]. The dangling bonds of the bottommost C atoms are always passivated by pseudo-H atoms. These demanding large supercell calculations (up to 3850 atoms) are currently made viable

with the use of GPU-based supercomputing resources at the National Energy Research Scientific Computing Center. The choice of k mesh depends on the supercell size. Based upon convergence tests, we choose the k mesh of $20 \times 20 \times 1$ for $(2 \times 2)\text{G}/(1 \times 1)\text{Si}$, $6 \times 6 \times 1$ for $(4 \times 4)\text{G}/(2 \times 2)\text{Si}$, $4 \times 4 \times 1$ for $(6 \times 6)\text{G}/(3 \times 3)\text{Si}$, $2 \times 2 \times 1$ for $(10 \times 10)\text{G}/(5 \times 5)\text{Si}$, $1 \times 1 \times 1$ for $(13 \times 13)\text{G}/(6 \times 6)\text{Si}$, $1 \times 1 \times 1$ for $(20 \times 20)\text{G}/(9 \times 9)\text{Si}$, and $1 \times 1 \times 1$ for $(26 \times 26)\text{G}/(12 \times 12)\text{Si}$. For bulk Pb, using a k mesh of $61 \times 61 \times 61$, we obtain a lattice constant of $a_{\text{pb}} = 5.015 \text{ \AA}$ (cf. the experimental values: 4.95004 \AA at 25°C [53] and 4.915 \AA at 0 K [54]), a cohesive energy of $E_{\text{coh}} = 3.324 \text{ eV}$ (cf. the experimental value: 2.029 eV [55]), and a bulk modulus of 42.01 GPa (cf. the experimental value: 42.97 GPa [56]). For freestanding Pb layers, we choose the k mesh $61 \times 61 \times 1$ or $51 \times 51 \times 1$ (see Sec. III).

Here, we need to clarify the word ‘‘amorphous’’ used below. Amorphous means ‘‘without a clearly defined form’’ or ‘‘lacking long-range order’’, e.g., in contrast to a periodic structure. In this work, we always use a periodic slab in a DFT calculation. Thus, especially for a smaller supercell, using the word amorphous is rather inappropriate, and instead we use the term ‘‘amorphous-like’’. For a sufficiently large supercell, e.g., $(13 \times 13)\text{G}/(6 \times 6)\text{Si}$, using a periodic slab to calculate amorphous surface systems is a reasonable approximation.

III. FREESTANDING Pb(111) MONOLAYER, Pb(111) BILAYER, AND PLUMBENE

Before analyzing the Pb layer intercalation next sections, it is necessary to first make an analysis for freestanding Pb layers because their lattice parameters determine the strain of a Pb layer matching SiC(0001) substrate, as described above. For a freestanding single Pb(111) plane layer (which is classified as ‘‘a monolayer;’’ see below), our DFT value of the equilibrium lattice constant is $a_0 = 3.290 \text{ \AA}$ from a k mesh of $61 \times 61 \times 1$ (cf. $a_0 = 3.295 \text{ \AA}$ from a k mesh of $51 \times 51 \times 1$), as shown in Fig. 2(a). Note that the Pb(111) monolayer lattice constant $a_0 = 3.290 \text{ \AA}$ has a decrease of 7.2% relative to a bulk Pb(111) slab with the surface lattice constant $a_{\text{pb}}/\sqrt{2} = 5.015/\sqrt{2} = 3.546 \text{ \AA}$. In this work, when analyzing the strain of a Pb(111) monolayer on SiC(0001), we use the lattice constant $a_0 = 3.290 \text{ \AA}$ but not the bulk value 3.546 \AA , as listed in Table I.

Next, let us analyze high-buckled (HB), low-buckled (LB), and planar (PL) honeycomb structures of Pb. These three structures correspond to large, small, and zero d values, respectively, where d is the interlayer spacing between two buckled single-plane layers forming a honeycomb structure [57,27]. As shown in Fig. 2(b), the curve (red with dots) of energy per unit cell versus the Pb honeycomb lattice constant a_0 indicates two phases corresponding to two energy minima. One is the HB phase at $a_0 = 3.519 \text{ \AA}$ with $d = 2.641 \text{ \AA}$. The blue curve with diamonds in Fig. 2(b) shows d versus a_0 . Note that this HB phase exactly corresponds to a freestanding Pb(111) bilayer [58], as indicated by the insets in Fig. 2(b). At $a_0 = 4.904 \text{ \AA}$, the LB phase has a small d value of 0.940 \AA and corresponds to plumbene with consistent lattice parameters with previous DFT calculations [26,31,41]. The HB phase is 0.972 eV lower than the LB phase in energy, and the phase

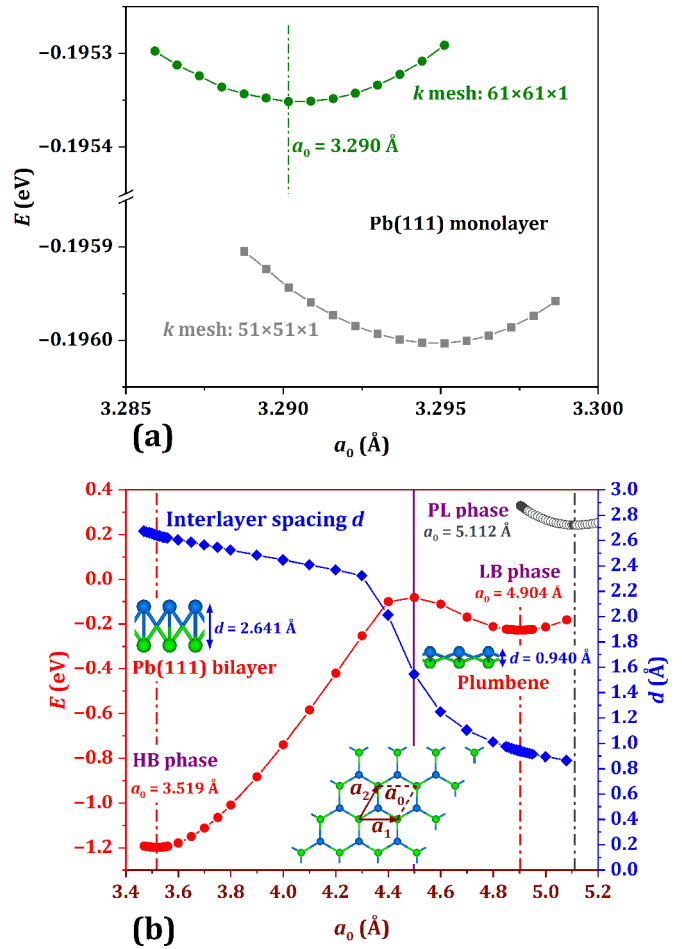


FIG. 2. (a) Energy (E) per unit cell vs lattice constant (a_0) of a Pb(111) monolayer (single-atom thick) from our DFT calculations using different k mesh of $51 \times 51 \times 1$ and $61 \times 61 \times 1$. (b) Energy (E) (red curve with dots or black curve with circles) per unit cell and interlayer spacing (d) (blue curve with diamonds) vs lattice constant (a_0) of a Pb honeycomb structure from our DFT calculations. The lower inset is the top view of the honeycomb structure for which the primitive cell is indicated by two lateral translation vectors \mathbf{a}_1 and \mathbf{a}_2 . The HB, LB, and PL phases are indicated. Two upper insets show the side views of Pb(111) bilayer and plumbene. The blue and green colors in these insets are used to identify two buckled single-atom-thick layers.

transition happens at $a_0 = 4.500 \text{ \AA}$ and $d = d_{\text{tr}} = 1.546 \text{ \AA}$ with an energy barrier of 0.145 eV , as indicated by the purple vertical line in Fig. 2(b). The PL phase (i.e., $d = 0$) is found at $a_0 = 5.112 \text{ \AA}$ with a 0.469-eV -higher energy than the LB phase, as shown by the curve with black circles in Fig. 2(b). Thus, among the three phases, the HB phase is thermodynamically most favorable, and the PL phase is most unfavorable.

Here, we need to make a clarification for use of the word monolayer. In the literature, the word monolayer is often used to describe a single-atom-thick layer, but sometimes also to describe a 2D material system composed of multiple buckled single-atom-thick layers. In this work, we use the word monolayer to describe any 2D structure with an interlayer spacing $d \lesssim d_{\text{tr}}$, e.g., we refer to a LB or PL honeycomb structure of Pb as a plumbene (or plumbene-like) monolayer. If a 2D

structure has two single-atom-thick layers satisfying $d \gtrsim d_{tr}$, we use the word “bilayer” to describe it, e.g., we refer to a HB honeycomb structure of Pb as a Pb(111) bilayer.

IV. Pb INTERCALATION

The thermodynamic favorability of an intercalated Pb structure can be analyzed by using the chemical potential [24], which is defined as

$$\mu = \frac{E_{tot} - E_{GSiC}}{P} - E_{gas,Pb}, \quad (3)$$

where E_{tot} is the total energy of the whole Pb intercalated slab, E_{GSiC} is the energy of ZLG-SiC substrate (without Pb), P is the total number of Pb atoms in the supercell, and $E_{gas,Pb}$ is the energy of one Pb atom in the gas phase. Replacing the reference energy $E_{gas,Pb}$ in Eq. (3) with the energy (σ_{Pb}) per Pb atom in bulk face-centered cubic (fcc) Pb crystal yields an alternative chemical potential:

$$\mu^* = \frac{E_{tot} - E_{GSiC}}{P} - \sigma_{Pb}. \quad (4)$$

The chemical potential μ^* in Eq. (4) is equivalent to the combination energy E_{comb} previously defined [59]. $\mu^* < 0$ ($\mu^* > 0$) indicates that the combination of intercalated Pb with the ZLG-SiC system from bulk Pb is exothermic (endothermic) and therefore the combined structure, i.e., the product, is more stable (unstable) than the reactants including the bulk Pb and ZLG-SiC substrate. For bulk fcc Pb, the chemical potential is $\mu = \mu_0 \equiv \sigma_{Pb} - E_{gas,Pb} = -E_{coh}$ and $\mu^* = 0$.

If P is the total number of Pb atoms in a supercell and N is the number of Si atoms in the perfect STL in this supercell, then the coverage of intercalated Pb is defined as $\theta = P/N$, i.e., the fraction of number of Pb atoms in the perfect STL. In experiments [8,16], the intercalation temperature (around 450 °C) is relatively low and the deintercalation occurs just 100 °C higher. This has led to several cycles of deposition-annealing to ensure that the intercalated Pb coverage reaches a steady-state value. Depending on the number of cycles and annealing temperature, the intercalated Pb can increase or decrease so that the coverage of intercalated Pb phases can be lower or higher than the starting phase. In our DFT calculations below, for simplicity, we always assume that the intercalated Pb coverage θ does not change from an initial configuration to its final configuration during relaxation.

For convenience of discussion below, we illustrate the fcc, bridge, hexagonal close-packed (hcp), and top sites on the STL of the SiC(0001) substrate in Fig. 1.

Our previous DFT calculations by using the $(4 \times 4)G/(2 \times 2)Si$ supercell [24] have already shown that the chemical potential of an intercalated Pb in the ZLG-STL gallery does not significantly depend on the thickness of graphene layers (SLG or only ZLG). Thus, we analyze the intercalated Pb structures for only ZLG-SiC(0001) system, i.e., we do not involve SLG in this work for any type of supercells.

A. $(2 \times 2)G/(1 \times 1)Si$

For this smallest supercell, we first relax three different initial configurations for each of which a 1×1 Pb(111) mono-

layer is intercalated (i.e., $P = 1$ and $\theta = P/N = 1/3$; see Table S1 in Appendix B with Supplemental Material [43]). Among them, we find that the configuration in Fig. S1(b) with intercalated Pb atom relaxed to a hcp site has the lowest μ value of -2.727 eV.

Then, we relax four different initial configurations for each of which a 1×1 plumbene-like monolayer is intercalated (i.e., $P = 2$ and $\theta = 2/3$; see Table S1). Relative to the relaxed configurations in Figs. S1(d) and S1(f), the configuration in Fig. S1(h) with two intercalated Pb atom relaxed to two bridge sites has the lowest μ value of -3.118 eV. Any plumbene-like monolayer in all these configurations is always almost planar after full relaxation.

Finally, we relax three different initial configurations for each of which a $1 \times 1_{R30}$ Pb(111)-like monolayer is intercalated (i.e., $P = 3$ and $\theta = 1$; see Table S1). As mentioned in Sec. II, the supercell $1 \times 1_{R30}$ of Pb(111)-like monolayer has the same orientation as SiC(0001) substrate, i.e., there is a rotation angle of 30° between primitive cells of Pb(111) and ZLG. A primitive cell of Pb(111) is indicated by a yellow rhombus in Fig. S1(i). After full relaxation, the $1 \times 1_{R30}$ Pb(111)-like monolayer in any of the three configurations is relaxed to a buckled monolayer with a 1×1 Pb(111) submonolayer on a 1×1 plumbene-like almost-planar submonolayer. The spacing between these two submonolayers is $s \approx 0.75 \text{ \AA}$ (cf. interlayer spacing $d = 0.940 \text{ \AA}$ between two buckled plane layers for freestanding plumbene in Sec. III). The configuration with the lowest μ value of -3.312 eV is shown in Fig. S1(l). We also note that relative to Fig. S1(j) with a slightly higher μ value of -3.309 eV, graphene in Fig. S1(l) has a slight shift which might be an artificial effect, as we discussed previously [51]. Recently, Yang *et al.* have assumed a buckled Pb(111) monolayer configuration similar to that in Fig. S1(j) in predicting electronic properties using a $(2 \times 2)G/(1 \times 1)Si$ supercell [22]. Here, we emphasize that the buckled Pb(111) monolayer is composed of a 1×1 Pb(111) submonolayer and a 1×1 planar plumbene submonolayer, as indicated by gray and black balls in Figs. S1(j) and S1(l).

B. $(4 \times 4)G/(2 \times 2)Si$

For this supercell, we first examine low-coverage configurations. For a Pb monomer (i.e., $P = 1$ and $\theta = 1/12$), we obtained a positive μ value of $+3.955$ eV. This indicates that the intercalation of such a single Pb atom is extremely unfavorable thermodynamically [24]. With increasing θ , μ decreases from a dimer ($\theta = 1/6$) with a μ value of -0.404 eV to a trimer (zigzaglike chain) ($\theta = 1/2$) with $\mu = -1.724$ eV to a tetramer ($\theta = 1/3$) with $\mu = -2.438$ eV (see Table S1). In Figs. S2(a) and S2(b), the initial and fully relaxed configurations with an intercalated 2×2 Pb(111) monolayer are illustrated. Such a uniformly distributed Pb monolayer has a significantly lower μ value of -2.693 eV than -2.438 eV of the above tetramer configuration with the same coverage $\theta = 1/3$.

By relaxing a configuration with an intercalated 3×3 Pb(111)-like monolayer ($\theta = 3/4$), we obtain a low μ value of -3.348 eV [see Figs. S2(c) and S2(d)]. Then, we place one extra Pb atom on top of a 3×3 Pb(111)-like monolayer

[Fig. S2(e)]. Such a Pb intercalant ($\theta = 5/6$) is finally relaxed to a Pb(111)-like Pb₅-ring monolayer with a small corrugation $c = 0.088 \text{ \AA}$, reflecting a slight amorphization [Fig. S2(f)], where the corrugation c is defined as the height difference between the highest atom and the lowest atom within a monolayer [51]. This Pb₅-ring monolayer has a slightly lower μ value of -3.356 eV , indicating that these structures are almost degenerate. When we relax a configuration by removing one Pb atom in a Pb₅-ring monolayer [Fig. S2(g)], we obtain a 3×3 Pb(111)-like monolayer [Fig. S2(h)]. Note that the 3×3 Pb(111)-like monolayers in Figs. S2(h) and S2(d) have the same μ but different Pb-SiC stackings. In addition, in order to see sensitivity of the coverage and local-defect dependence, we relaxed more configurations, e.g., constructing various initially intercalated structures by removing or adding Pb atoms from or on top of a Pb(111)-like Pb₅-ring monolayer, as listed in Table S1. These fully relaxed configurations have the μ values around -3.3 eV , slightly higher than -3.356 eV for the above perfect Pb₅-ring monolayer.

We relax an intercalated 4×4 Pb(111) monolayer [Fig. S2(i)]. The configuration with such a higher coverage ($\theta = 4/3$) is finally relaxed to an amorphous-like Pb bilayer structure with $\mu = -3.260 \text{ eV}$ [Fig. S2(j)]. This bilayer is composed of two Pb monolayers: a 7-Pb-atom monolayer on top of a 9-Pb-atom monolayer (the similar relaxation behavior was also found for Dy intercalation [51]), with an average interlayer spacing of 2.807 \AA .

We also relax an intercalated $2 \times 2_{R30}$ Pb(111)-like monolayer ($\theta = 1$) [Fig. S2(k)]. After full relaxation, this $2 \times 2_{R30}$ Pb(111)-like monolayer is relaxed to a buckled monolayer with a 2×2 Pb(111)-like submonolayer on a 2×2 plumbene-like almost-planar submonolayer [Fig. S2(l)]. The spacing between these two submonolayers is $s \approx 0.70 \text{ \AA}$. The Pb structure in Fig. S2(l) is similar to that in Fig. S1(j) or S1(l), and the μ value of -3.298 eV for the former is slightly higher than -3.312 or -3.309 eV for the latter.

Next, we try to see if a plumbene-like monolayer can form. We first choose a plumbene-like monolayer ($\theta = 2/3$) in any initial configuration. By changing the positions of Pb atoms of the plumbene-like monolayer, we build seven different initial configurations. After full relaxation, five of the seven configurations are relaxed to amorphous-like Pb monolayers [see Fig. S3(b) for an example], and two of them are relaxed to a Pb(111)-like monolayer with a vacancy [see Fig. S3(d) for an example with a dashed circle representing a vacancy], as listed in Table S1. The μ values of all these seven configurations are around -3.2 eV . Here, it should be mentioned that we also relax multiple configurations (Table S1) for which a 3×3 Pb(111)-like monolayer with vacancies is the intercalant. These fully relaxed configurations also have the μ values around -3.2 eV . This again indicates the degeneracy of these amorphous-like and Pb(111)-like structures.

Then, we try to relax two initial configurations with a 2×3 Pb(110)-like monolayer ($\theta = 1/2$) [Figs. S3(e) and S3(g)], where “ 2×3 ” stands for a rectangular supercell (indicated by a dashed orange rectangle) equivalent to a rhombic supercell (each white rhombus), and its side lengths are in units of strained long and short lattice constants of Pb(110) [58]. After full relaxation, these Pb(110)-like monolayers become distorted and somewhat plumbene-like [Figs. S3(f) and

S3(h)], but both have a higher μ value of -2.945 eV relative to the above Pb(111)-like or amorphous-like configurations with the μ values below -3 eV . In Fig. S3(f) or S3(h), we show a 30° rotated primitive cell (dashed yellow rhombus) of plumbene relative to the graphene unit cell, i.e., the orientation of the plumbene primitive cell is the same as that of SiC(0001).

For higher-coverage intercalation, we first relax two initial configurations with a 3×3 Pb(111)-like bilayer ($\theta = 3/2$) of different Pb-SiC stackings [Figs. S3(i) and S3(k)] but obtain the almost-equal μ values of -3.304 and -3.307 eV [Figs. S3(j) and S3(l)]. Then, we relax two initial configurations with a 3×3 Pb(111)-like monolayer on a Pb₅-ring monolayer ($\theta = 19/12$) of different Pb-SiC stackings but obtain the same μ value of -3.281 eV (Table S1).

C. $(6 \times 6)\text{G}/(3 \times 3)\text{Si}$

For this supercell, we first consider the intercalation of a 5×5 Pb(111) monolayer ($\theta = 25/27$) [Fig. S4(a)]. After full relaxation, we obtain a Pb(111)-like monolayer with a single-Pb-atom protrusion of about 0.9 \AA relative to other Pb atoms in the Pb monolayer [Fig. S4(b)]. Then, we remove one, two, three, four, and five Pb atoms from the Pb monolayer in Fig. S4(b) to construct five structures ($\theta = 24/27, 23/27, 22/27, 21/27, \text{ and } 20/27$), as shown in Figs. S4(c), 6(e), 6(g), 6(i), and 6(k), respectively, where the vacancies after the removal of the Pb atoms are indicated by dashed red circles. In Fig. S4(k), the 5×5 Pb(111) monolayer after removing the five Pb atoms becomes a 4×5 Pb(111)-like ribbon equivalently. After full relaxation, an evolution from Pb(111)-like to amorphous-like Pb monolayer can be observed from Fig. S4(b) to Fig. S4(d) to Fig. S4(f) to Fig. S4(h) to Fig. S4(j) to Fig. S4(l). With decreasing θ , the μ value first decreases and then increases. Among the six configurations in Fig. S4, a chemical potential minimum $\mu = -3.364 \text{ eV}$ appears at $\theta = 22/27 \approx 0.8148$ [Fig. S4(h)]. However, the μ values of all these configurations have small differences ($< 0.08 \text{ eV}$).

Instead of a 4×5 Pb(111)-like ribbon, we further remove one row and then the monolayer becomes a 4×4 Pb(111)-like island ($\theta = 16/27$) [Fig. S5(a)], where the “island” means that there are four missing rows around the 4×4 2D Pb(111) cluster. We relax such a Pb island and obtain an amorphous-like Pb monolayer [Fig. S5(b)], but $\mu = -3.157 \text{ eV}$ is higher than all above configurations in Fig. S4.

Relaxing a 3×3 plumbene-like monolayer ($\theta = 2/3$) [Fig. S5(c)], we obtain the plumbene-like monolayer in Fig. S5(d). This plumbene-like monolayer has a μ value of -3.079 eV , which is close to $\mu = -3.087, -3.085, \text{ and } -3.118 \text{ eV}$ for the plumbene-like monolayers in Figs. S1(d), S1(f), and S1(h), respectively. Also note that all these plumbene-like monolayers are planar.

We also relax a $3 \times 3_{R30}$ Pb(111) monolayer ($\theta = 1$) [Fig. S5(e)]. After full relaxation, this $3 \times 3_{R30}$ Pb(111) monolayer is relaxed to a buckled monolayer with a 3×3 Pb(111) submonolayer on a 3×3 plumbene-like almost-planar submonolayer [Fig. S5(f)]. The spacing between these two submonolayers is $s \approx 0.72 \text{ \AA}$. The Pb structure in Fig. S2(l) is similar to that in Fig. S2(l), S1(j), or S1(l), and the μ value of -3.298 eV is the same as that for Fig. S2(l).

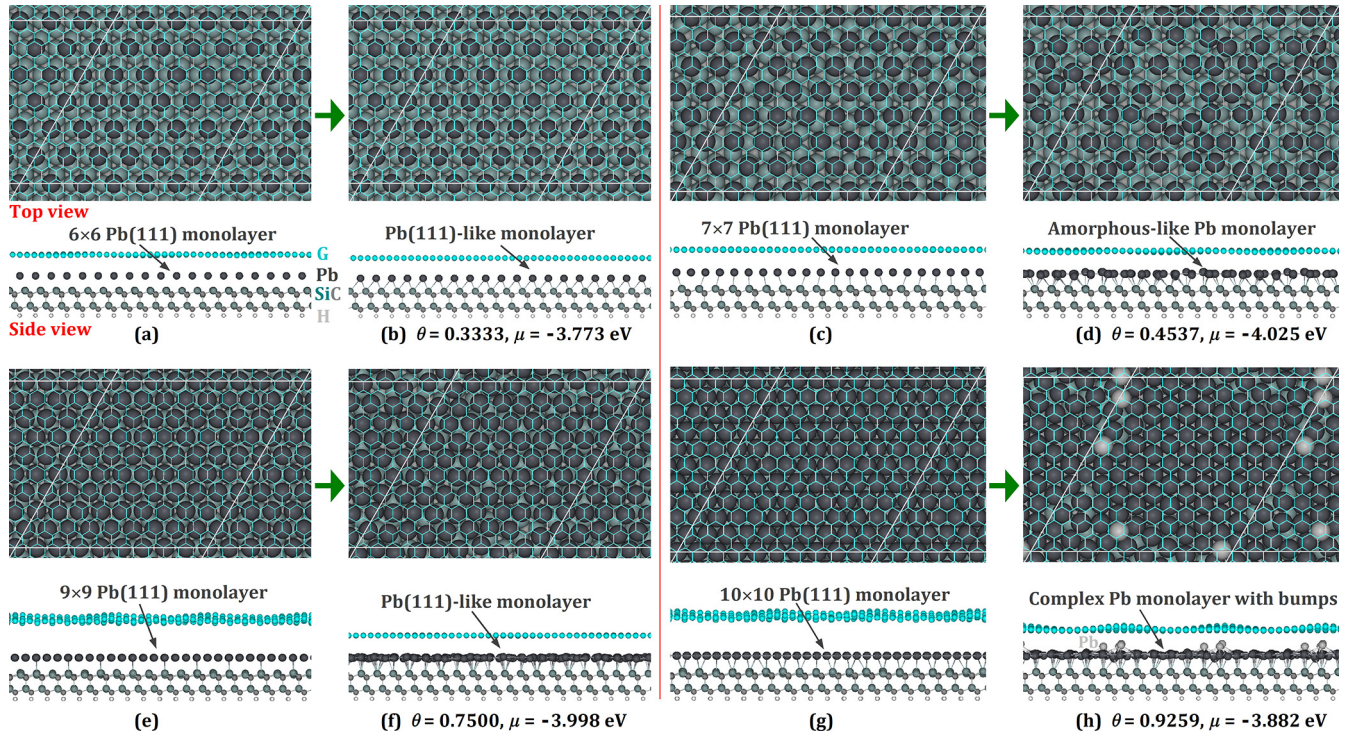


FIG. 3. Top and side views from initial (a), (c), (e), and (g) to fully relaxed (b), (d), (f), and (h) configurations from our DFT calculations by using a $(13 \times 13)\text{G}/(6 \times 6)\text{Si}$ supercell (each white rhombus), as indicated by the thick olive arrows. The thin cyan mesh of each top view represents the ZLG. The structure of intercalated Pb in an initial or fully relaxed configuration is indicated by the black arrow. DFT chemical potentials (μ) and intercalated Pb coverages (θ) of fully relaxed configurations are also provided. The intercalated Pb coverage θ for any initial configuration is always the same as its final fully relaxed configuration. For more details, see the text as well as Appendix B with Table S1. Similar statements apply to all the following figures and will no longer be repeated.

D. $(10 \times 10)\text{G}/(5 \times 5)\text{Si}$

For this supercell, we first relax four configurations in Fig. S6. They are a 6×6 Pb(111) monolayer ($\theta = 36/75 = 0.48$) [Fig. S6(a)], a 7×7 Pb(111) island ($\theta = 49/75 \approx 0.6533$) [Fig. S6(c)], a 7×7 Pb(111) monolayer ($\theta = 49/75 \approx 0.6533$) [Fig. S6(e)], and a 8×7 Pb(111)-like ribbon ($\theta = 56/75 \approx 0.7467$) [Fig. S6(g)]. After full relaxation, each of them becomes an amorphous-like Pb monolayer, as shown in Figs. S6(b), S6(d), S6(f), and S6(h). Overall, with increasing θ , the μ value decreases from -3.18 to -3.37 to -3.45 eV. For two initial configurations, the 7×7 Pb(111) island and the 7×7 Pb(111) monolayer with the same $\theta = 49/75$, the positions of Pb atoms in their fully relaxed amorphous-like structures are different, but they have almost the same μ values of -3.372 and -3.374 eV. This indicates the sensitivity of positions of Pb atoms but the insensitivity of chemical potentials to the initial configuration for the amorphization.

When we relax an intercalated 8×8 Pb(111) island ($\theta = 64/75 \approx 0.8533$) [Fig. S7(a)], an 8×8 Pb(111)-like monolayer is obtained with a lower μ value of -3.484 eV [Fig. S7(b)] than -3.451 eV of the amorphous-like structure [Fig. S6(h)] from the above 8×7 Pb(111)-like ribbon. If we remove one Pb atom from the above fully relaxed 8×8 Pb(111)-like monolayer ($\theta = 63/75 = 0.84$) [Fig. S7(c)], we find that the optimized Pb(111)-like monolayer with a vacancy [indicated by one dashed red circle in Fig. S7(d)] does not change its μ value. If we remove three Pb atoms [Fig.

S7(e)], we find that the μ value of the optimized Pb(111)-like monolayer with three vacancies [indicated by three dashed red circle in Fig. S7(f)] has a slight decrease to -3.467 eV. This behavior is in contrast to a Pb(111) monolayer on a Pb(111) surface, where the μ values are significantly different for Pb monolayers with and without a Pb vacancy due to the nonzero vacancy formation energies [24]. In experiments, the change of 1 meV in chemical potential corresponds to a temperature change of about 10 K. The experimental intercalation temperatures vary from 200 to 450 °C [16], and thus our results indicate that all the above phases with the μ values around -3.4 eV are effectively degenerate.

E. $(13 \times 13)\text{G}/(6 \times 6)\text{Si}$

We first relax four $l \times l$ Pb(111) monolayers [Figs. 3(a), 3(a), 3(e), and 3(g)]. For $l = 6$ ($\theta = 36/108 \approx 0.3333$), the fully relaxed structure is still a Pb(111)-like monolayer with $\mu = -3.773$ eV [Fig. 3(b)]. For $l = 7$ ($\theta = 49/108 \approx 0.4537$), the fully relaxed structure is an amorphous-like monolayer with $\mu = -4.025$ eV [Fig. 3(d)]. For $l = 9$ ($\theta = 81/108 = 0.75$), the fully relaxed structure is again a Pb(111)-like monolayer with $\mu = -3.998$ eV [Fig. 3(f)]. For $l = 10$ ($\theta = 100/108 \approx 0.9259$), the fully relaxed structure is a complex Pb monolayer [a rotated Pb(111)-like monolayer with amorphous-like regions and bumps] with $\mu = -3.882$ eV [Fig. 3(h)]. Note that the Pb bumps on the Pb monolayer in

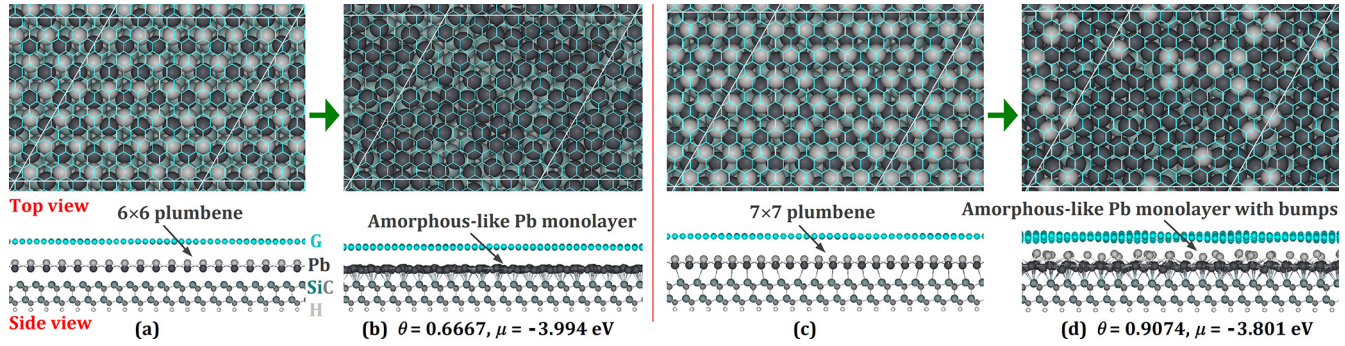


FIG. 4. Top and side views from initial (a), (c) to fully relaxed (b), (d) configurations from our DFT calculations by using a $(13 \times 13)\text{G}/(6 \times 6)\text{Si}$ supercell.

Fig. 3(h) induce the graphene corrugation of about 0.83 \AA . Thus, the fully relaxed structure strongly depends on the dimension l of the initial Pb(111) monolayer. It seems that this dependence originates from the strain ε_{pb} . For $l = 6$, the Pb-SiC strain $\varepsilon_{\text{pb}} = +63.0\%$. See Table I for a list of the strain ε_{pb} in an $l \times l$ Pb layer relative to substrate SiC(0001) along the $\sqrt{3}a_{\text{SiC}} \times \sqrt{3}a_{\text{SiC}}$ unit cell. Such a large tensile lateral strain can cause the stretching between Pb atoms to far exceed the elastic limit and therefore very weak Pb-Pb interactions so that the positions of Pb atoms after relaxation are mainly determined by overall vertical Pb-substrate (both Pb-graphene and Pb-SiC) electronic interactions. Consequently, the Pb(111) monolayer structure can remain at such a very high tensile strain and a relatively low Pb coverage. In this case, we initially place all Pb atoms at fcc sites and the positions of Pb atoms nearly do not change after relaxation. It is expected that initially placing the Pb atoms at other sites, e.g., fcc sites, can reduce the chemical potentials, but the fully relaxed Pb monolayer will be still Pb(111)-like, as analyzed in Secs. IV A and IV B for small supercells $(2 \times 2)\text{G}/(1 \times 1)\text{Si}$ and $(4 \times 4)\text{G}/(2 \times 2)\text{Si}$, respectively. For relatively intermediate or small tensile strain as well as intermediate Pb coverages, e.g., $\varepsilon_{\text{pb}} = +39.7\%$ for $l = 7$ and $\varepsilon_{\text{pb}} = +8.6\%$ for $l = 9$, more significant Pb-Pb interactions due to the reduced nearest-neighbor distances together with Pb-substrate electronic interactions can result in complex amorphous-like structure. For $l = 10$, $\varepsilon_{\text{pb}} = -2.2\%$, i.e., the lateral strain is compressive. Such compression, caused by the relatively too short nearest-neighbor distances at a higher Pb coverage, can push the extra Pb atoms to the top (forming the Pb bumps) to reach a local energy minimum by partly rotating Pb(111) orientation and partly becoming disordered during the relaxation.

Then, we relax two $l \times l$ plumbene monolayers [Figs. 4(a) and 4(b)], where the plumbene is initially taken to be the LB phase with the interlayer spacing $d = 0.940 \text{ \AA}$, as shown in Fig. 2(b). For $l = 6$ ($\theta = 72/108 \approx 0.6667$), the fully relaxed structure is an amorphous-like monolayer with $\mu = -3.994$ eV [Fig. 4(b)]. For $l = 7$ ($\theta = 98/108 \approx 0.9074$), the fully relaxed structure is an amorphous-like Pb monolayer (with Pb bumps) with $\mu = -3.801$ eV [Fig. 4(d)]. Also note that the Pb bumps on the amorphous-like Pb monolayer in Fig. 4(d) induce the graphene corrugation of about 1.22 \AA . The reason for the very different fully relaxed structures might originate

from the different plumbene-SiC strains at the different Pb coverages. For $l = 6$, the plumbene-SiC strain $\varepsilon_{\text{pb}} = +9.3\%$. See Table I for a list of the strain ε_{pb} in plumbene relative to substrate SiC(0001). The tensile strain can stretch the initial plumbene into an amorphous-like phase [Fig. 4(b)] at the relatively low Pb coverage. For $l = 7$, the plumbene-SiC strain $\varepsilon_{\text{pb}} = -6.3\%$, i.e., the strain becomes compressive and then such compression between Pb atoms at a higher Pb coverage can push the extra Pb atoms to the top (forming the Pb bumps) to reach a local energy minimum by becoming disordered during the relaxation [Fig. 4(d)].

In order to further search for possible formation of plumbene-like monolayers, we relax a 6×9 Pb(110) monolayer ($\theta = 54/108 = 0.5$) [Fig. 5(a)], where “ 6×9 ” stands for an equivalent rectangular supercell (for more details, see Sec. IV B). By monitoring the optimization process, a 30° rotated plumbene-like monolayer can indeed be observed during relaxation, where the primitive cell of the honeycomb lattice of Pb is around 6 \AA , which is significantly larger than 4.904 \AA for freestanding plumbene, and the orientation is approximately the same as that of SiC(0001), as illustrated in Fig. 5(b). Such a stretched, more regular plumbene-like monolayer has a μ value of -3.928 eV. However, it is unstable and is finally relaxed to a more amorphous version with an only 0.024 eV lower μ value of -3.952 eV, as shown in Fig. 5(c). Here, we also note the similarity between the structure in Fig. 5(c) from the large supercell of $(13 \times 13)\text{G}/(6 \times 6)\text{Si}$ and the structure in Fig. S3(f) or S3(h) from a small supercell of $(4 \times 4)\text{G}/(2 \times 2)\text{Si}$, where each plumbene-like monolayer is 30° rotated and has a significant structural distortion compared to a regular honeycomb lattice.

In order to search for configurations with possible lowest μ values, we change θ by removing Pb atoms from or adding Pb atoms on an already optimized Pb(111)-like or amorphous-like Pb monolayer. We find that these configurations with varying θ have very close μ values around -4.0 eV (Table S1), indicating their degeneracy. An example is that the configuration ($\theta = 80/108 \approx 0.7407$) [Fig. 6(a)] with a vacancy (dashed red circle) by removing one Pb atom from the 9×9 Pb(111)-like monolayer in Fig. 3(f) does not change its μ value of -3.998 eV. The configurations in Fig. 6(a) or 3(f) have the lowest μ value within all Pb(111)-like monolayer structures that we consider in this work, while the amorphous-like Pb monolayer ($\theta = 44/108 \approx 0.4074$) [Fig. 6(b)] has the

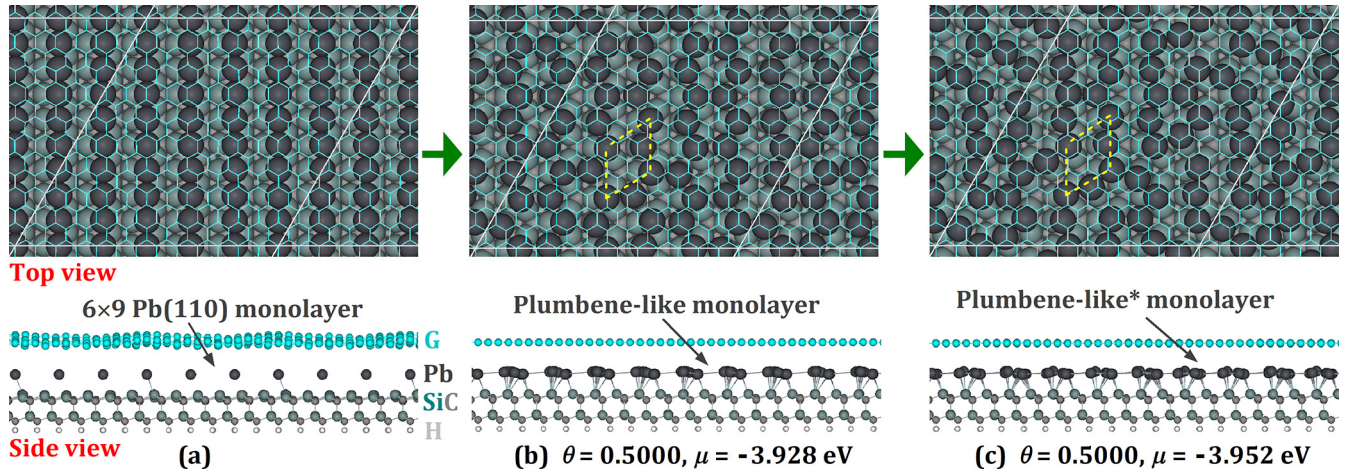


FIG. 5. Top and side views of initial (a), middle (b), and final fully relaxed (c) configurations from our DFT calculations by using a $(13 \times 13)\text{G}/(6 \times 6)\text{Si}$ supercell. An asterisk (*) after the word “plumbene-like” in (c) indicates a larger structural distortion compared to a more regular honeycomb lattice in (b). The dashed yellow rhombus indicates a 30° rotated plumbene primitive cell.

lowest μ value of -4.043 eV in all structures [16]. That is, the Pb(111)-like monolayer structure in Fig. 6(a) or 3(f) has the μ value only 0.045 eV higher than the amorphous-like structure in Fig. 6(b). In addition, as useful information, e.g., to compare with experimental data, for these two typical configurations with the lowest μ values we also show the Pb-graphene and Pb-STL interlayer spacings: 3.76 and 2.68 Å in Fig. 6(a), as well as 3.60 and 2.38 Å in Fig. 6(b), respectively. These values are very close to the measured results in recent experiments: the Pb-graphene interlayer spacing 3.67 Å and the Pb-STL interlayer spacing 2.72 Å [15]. We also note that all monolayers (including graphene, Pb, and STL) in these two configurations are almost flat with the very weak corrugations (< 0.5 Å) [16].

Finally, we relax two higher-coverage $l \times l$ Pb(111) bilayers [Figs. 7(a) and 7(c)]. For $l = 9$ ($\theta = 162/108 = 1.5$), the fully relaxed structure is still a Pb(111)-like bilayer with $\mu = -3.605$ eV [Fig. 7(b)]. The corrugations (< 0.1) of monolayers in this structure are very weak, except the top Pb monolayer has a slightly larger corrugation of about 0.3 Å. The interlayer spacings on average are $d_1 = 3.62$ Å, $d_2 = 2.75$ Å, and $d_3 = 2.63$ Å between top Pb monolayer and graphene, between two Pb monolayers, and between bottom Pb monolayer and STL, respectively. For $l = 10$ ($\theta = 200/108 \approx 1.8519$), the fully relaxed structure is a structure of amorphous-like Pb multiple layers with $\mu = -3.485$ eV [Fig. 7(d)]. These higher-coverage configurations have significantly higher μ values around -3.5 eV than the above lower-coverage configurations around -4.0 eV. This indicates that the intercalation of such Pb multilayers is relatively unfavorable thermodynamically. Such a result is consistent with previous experimental observations that the intercalated Pb monolayers rather than higher Pb coverages are very stable [7–12]. This behavior implies that the sum ($\Phi_{\text{PbG}} + \Phi_{\text{PbSiC}}$) of Pb-graphene and Pb-SiC interlayer interactions for the system with one intercalated Pb monolayer is stronger than the sum ($\Phi_{\text{PbPb}} + \Phi_{\text{GSiC}}$) of Pb-Pb and ZLG-SiC interlayer interactions (for an illustration with more details, see Appendix C). However, a precise quantitative analysis of

energy decomposition at equilibrium positions of Pb layers would be challenging [59].

F. $(20 \times 20)\text{G}/(9 \times 9)\text{Si}$

For this larger supercell, we only consider one configuration, an intercalated 14×14 Pb(111)-like monolayer ($\theta = 196/243 \approx 0.8066$) [Fig. S8(a)]. Its fully relaxed structure is still a 14×14 Pb(111)-like monolayer [Fig. S8(b)]. The chemical potential $\mu = -3.955$ eV is slightly higher than the lowest μ value of -3.998 eV for the Pb(111)-like monolayer in Fig. 6(a) or 3(f). For the fully relaxed structure in Fig. S8(b), we note that the intercalated Pb monolayer is very flat, but the graphene layer above it has a strong wavelike corrugation of about 4.0 Å. This behavior is not surprising, considering the laterally compressed graphene with a compressive strain $\varepsilon_{\text{G}} = -2.1\%$ in contrast to the positive ε_{G} values for all other supercells listed in Table I. Also, a relatively small tensile strain $\varepsilon_{\text{Pb}} = +4.8\%$ in a 14×14 Pb(111) monolayer (see Table I) is not expected to significantly affect the strain in the top graphene layer. For a positive ε_{G} value (i.e., tensile strain), the graphene layer is stretched, and then strong corrugations are not expected, as described in the above sections.

G. $(26 \times 26)\text{G}/(12 \times 12)\text{Si}$

For this large supercell, we only select one initial configuration, a 13×13 plumbene monolayer ($\theta = 338/432 \approx 0.7824$) [Fig. 8(a)]. Our purpose in selecting this configuration is still to search for possible plumbene formation when a supercell is sufficiently large. After full relaxation, we obtain an amorphous-like Pb monolayer with a three-atom protrusion [Fig. 8(b)]. Such an amorphous-like Pb monolayer has a rather lower μ value of -3.983 eV, which is close to the lowest value -4.043 eV [Fig. 6(b)], even though a three-atom protrusion appears during the relaxation.

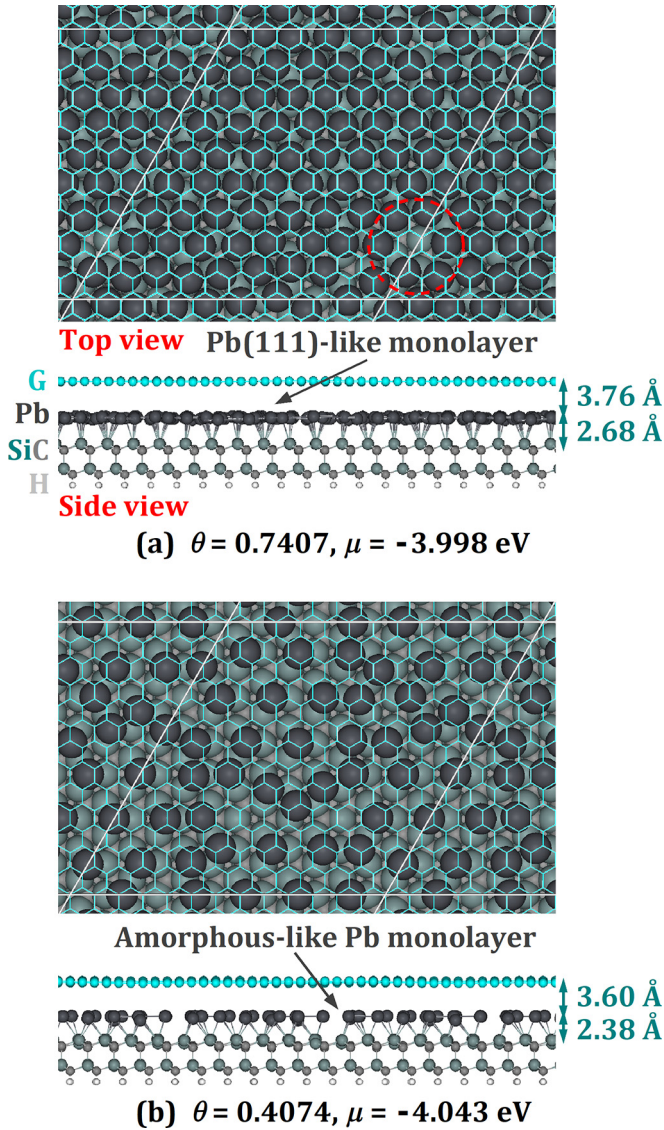


FIG. 6. Top and side views of two thermodynamically most favorable configurations from our DFT calculations by using a $(13 \times 13)G/(6 \times 6)Si$ supercell. (a) A 9×9 Pb(111)-like monolayer with a vacancy indicated by a dashed circle. This structure is energetically degenerate with the structure in Fig. 3(f) without the vacancy and they have the same lowest chemical potential (-3.998 eV) among all of Pb(111)-like structures in this work. (b) An amorphous-like Pb monolayer with the lowest chemical potential (-4.043 eV) in all configurations in this work. The DFT chemical potentials (μ), the intercalated Pb coverages (θ), and the interlayer spacings between graphene and the STL are indicated.

V. DISCUSSION

To compare the thermodynamic favorability of various intercalated Pb structures, in Fig. 9 we plot the chemical potential (μ) of Pb as a function of Pb coverage θ for 91 configurations calculated in the above sections. There are many Pb structures with their μ values below the Pb bulk value $\mu_0 = -E_{\text{coh}} = -3.324$ eV (or equivalently below $\mu^* = 0$). The μ values below μ_0 (or $\mu^* < 0$) reflect a preference of these intercalated Pb structures against the formation of large

Pb islands supported on top graphene, as observed in experiments [7–13]. Overall, the configurations with lowest μ values are from the low-strain supercell calculations (see Fig. 9): circles from $(13 \times 13)G/(6 \times 6)Si$ with $\varepsilon_G = +0.4\%$, the hexagon from $(20 \times 20)G/(9 \times 9)Si$ with $\varepsilon_G = -2.1\%$, and the dot from $(26 \times 26)G/(12 \times 12)Si$ with $\varepsilon_G = +0.4\%$. As analyzed above, the lowest μ value of -4.043 eV is found at a Pb coverage $\theta \approx 0.4047$, corresponding to an amorphous-like Pb monolayer [Fig. 6(b)].

As mentioned in Sec. IV A, in predicting electronic properties, Yang *et al.* [22] have recently used a $(2 \times 2)G/(1 \times 1)Si$ supercell by assuming an intercalated buckled Pb(111) monolayer similar to that in Fig. S1(j). However, the μ value of such a Pb monolayer is 0.734 eV higher, relative to the most favorable amorphous-like Pb monolayer in Fig. 6(b). Thus, we suggest a reconsideration of the predicted electronic properties by using, e.g., a more favorable amorphous-like Pb monolayer versus the above-assumed buckled Pb(111) monolayer, which is expected to be unobservable in experiments due to the significantly higher μ value.

In Fig. 9, to easily identify the structures, we use blue, olive, red, and pink colors to stand for Pb(111)-like, amorphous-like, plumbene-like, and Pb(111)/plumbene-like structures, respectively, where “Pb(111)/plumbene-like” denotes a buckled Pb(111) monolayer appearing as a Pb(111)-like monolayer on a plumbene-like monolayer. As shown in Fig. 9, the red or pink colored symbols corresponding to the smaller supercells with higher-strained ZLG ($\varepsilon_G = +8.8\%$) appear above the horizontal line $\mu = \mu_0$ (or $\mu^* = 0$), indicating that these plumbene-related structures are not favorable thermodynamically, relative to a large Pb island supported on top of graphene. A red circle corresponding to the larger $(13 \times 13)G/(6 \times 6)Si$ supercell with low-strained ZLG ($\varepsilon_G = +0.4\%$) appears far below the horizontal line $\mu = \mu_0$, indicating that this plumbene-like structure is rather favorable thermodynamically. However, we need to emphasize that such a plumbene-like structure is lattice distorted relative to the standard honeycomb lattice in plumbene, as shown in Fig. 5(c).

Experimentally, one of the challenges is to determine the exact coverage of the intercalated metal, which in most cases is assumed to be at saturation. Our extensive theoretical studies in this work show a very important dependence of overall decreasing chemical potential with increasing intercalated Pb coverage, which affects the exact subsurface phase stability in different experiments. A similar relation has been seen also in the DFT calculations of Dy intercalation for SLG on SiC(0001) [60].

Finally, we need to mention several caveats for the above analysis. As described in the above sections, the fully relaxed configuration in a DFT calculation can depend significantly on initially selected Pb configuration, given a Pb coverage within a specified supercell. In principle, to search for a reliable global energy minimum as well as a possible metastable configuration like a plumbene-like structure, as many initial configurations as possible are required. Due to the large computation expense and limitations of computational resources, we only choose about 100 configurations, as listed in Table S1. These configurations are selected on a case-by-case basis, e.g., we choose θ around 0.8 due to the low-strain ε_{pb} value

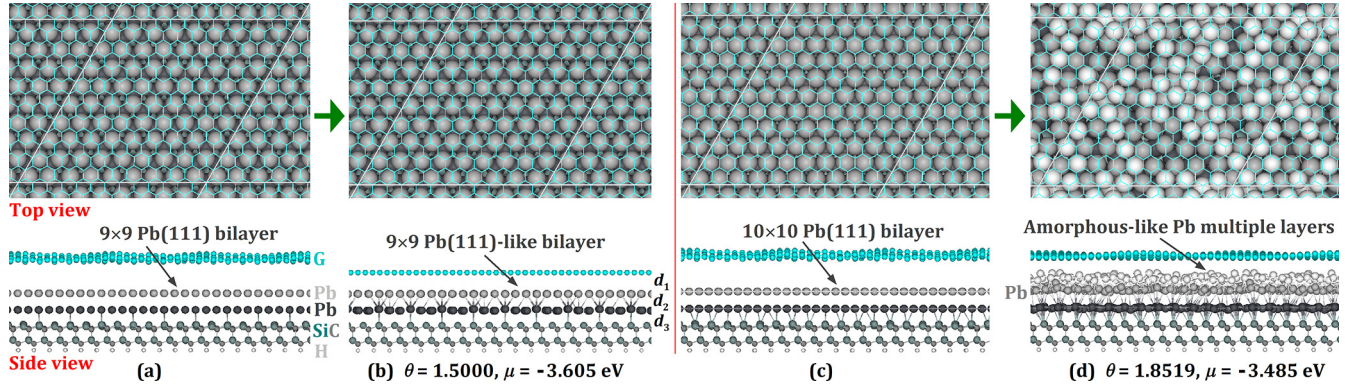


FIG. 7. Top and side views of initial (a), (c) and fully relaxed (b), (d) configurations from our DFT calculations by using a $(13 \times 13)G/(6 \times 6)Si$ supercell. In (b), $d_1 = 3.62$ Å, $d_2 = 2.75$ Å, and $d_3 = 2.63$ Å are the interlayer spacings on average between top Pb monolayer and graphene, between two Pb monolayers, and between bottom Pb monolayer and STL, respectively.

in a Pb(111) layer and θ around 0.4 due to the low-strain ε_{Pb} value for a plumbene-like monolayer (see Table I for listed ε_{Pb} values), as shown in Fig. 9. Particularly, during the search for possible plumbene-like structures, we only choose a limited number of initial configurations within a few types of supercells in this work. Therefore, without relaxing more selected initial configurations, which would be more computationally demanding, we cannot rule out the possibility of obtaining additional favorable plumbene-like structures, e.g., with higher Pb coverages, as observed in recent experiments [13].

VI. CONCLUSION

In conclusion, we have performed extensive first-principles DFT analysis for intercalated Pb structures under buffer-layer graphene on SiC(0001). In our calculations, we consider seven types of supercells to analyze the dependence of intercalation on the strain conditions determined by the different supercell lateral sizes. By comparing the chemical

potentials of intercalated Pb structures, we find that the amorphous-like Pb monolayers from a $(13 \times 13)G/(6 \times 6)Si$ supercell with a lowest lateral tensile strain of +0.4% are thermodynamically most preferred, while Pb(111)-like monolayers can have very close chemical potentials to these amorphous-like Pb monolayers and therefore they are almost energetically degenerate. The structures from smaller supercells, $(10 \times 10)G/(5 \times 5)Si$, $(6 \times 6)G/(3 \times 3)Si$, $(4 \times 4)G/(2 \times 2)Si$, and $(2 \times 2)G/(1 \times 1)Si$ with a higher lateral tensile strain of +8.8%, are also somewhat degenerate although with higher chemical potentials and larger differences between them. This extensive study of intercalated phase stability as a function of the supercell size also incorporates a wide range of coverages. Other Pb intercalated phases of different structures are found with similar chemical potentials. These phases can be accessed experimentally, based on studies of Pb intercalation kinetics with a range of experimental techniques such as STM, LEED, and x-ray photoelectron spectroscopy [11,12,16].

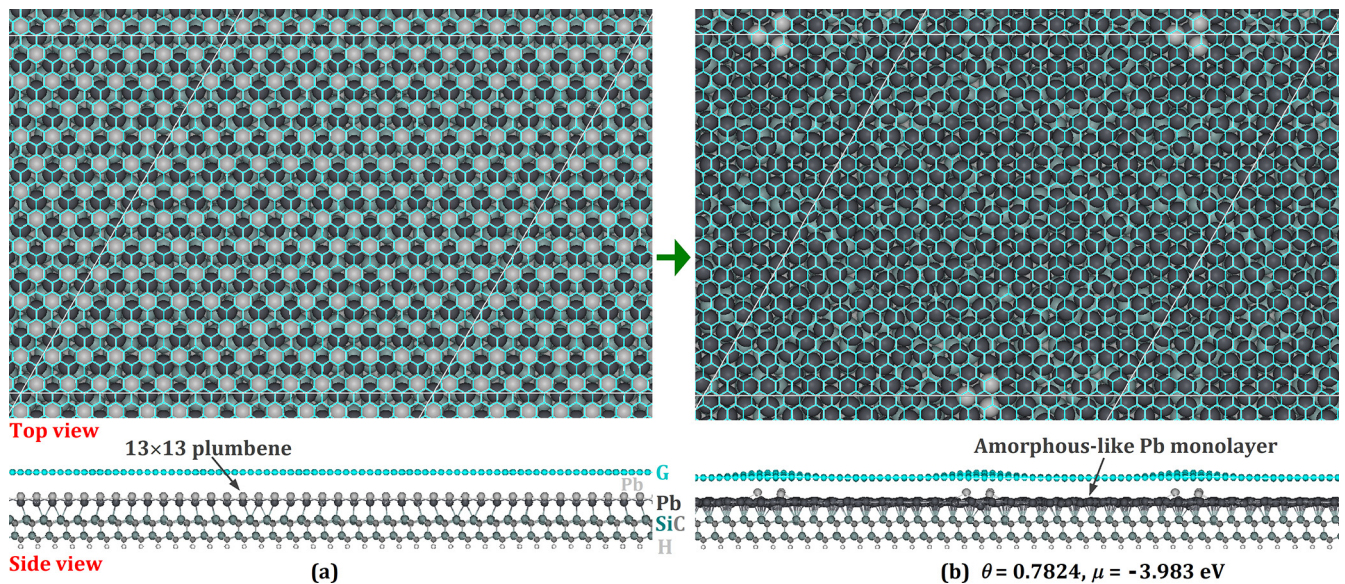


FIG. 8. Top and side views of initial (a) and fully relaxed (b) configurations from our DFT calculations by using a $(26 \times 26)G/(12 \times 12)Si$ supercell.

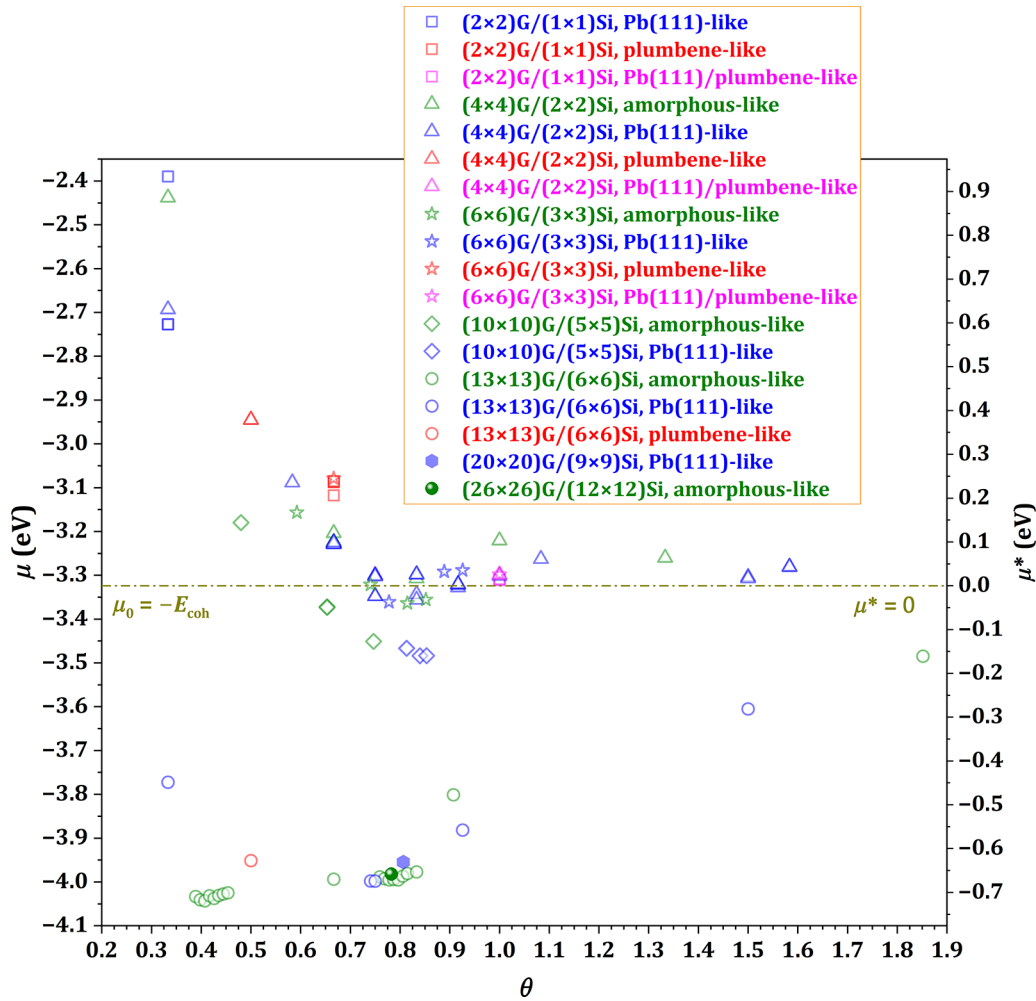


FIG. 9. DFT chemical potentials (μ or μ^*) of 91 intercalated Pb structures vs Pb coverage θ from 0.2 to 1.9. Seven types of supercells with varying lateral sizes are identified by different symbols. Blue, olive, red, and pink colors stand for Pb(111)-like, amorphous-like, plumbene-like, and Pb(111)/plumbene-like structures, respectively. The dashed-dotted horizontal line indicates the chemical potential $\mu_0 = -E_{\text{coh}}$ (i.e., $\mu^* = 0$) for bulk Pb, where $E_{\text{coh}} = 3.324$ eV is the cohesive energy of bulk Pb from our DFT calculation.

Despite the very large size of a Pb atom, its intercalation occurs at the relatively low temperature of about 450 °C, while deintercalation and full Pb desorption occurs at about 650 °C. Having these three competing processes (intercalation, deintercalation, and desorption), which are so close in temperature, implies very large Pb mobility between atop and below graphene. This can readily generate distinct intercalated phases of different coverage and ordering. The current extensive theoretical studies where numerous Pb subsurface structures were found, depending on variable unit cell, coverage, and chemical potential, confirm these experimentally observed facile kinetic exchanges of Pb atoms between subsurface and top locations. This behavior is consistent with several STM studies where small domains of different unit cells, of hexagonal or stripe symmetry, usually coexist within areas of about 40 nm in lateral size. Surface-diffraction measurements of spot profiles from the intercalated Pb layer also have low intensity [7,9–11]. The easy interchange of different subsurface phases within the very large variation in coverage of all the ones studied here also supports the likelihood that an amorphous

layer can easily form in this system. The amorphization of an intercalated 2D Pb layer will be advantageous for the realization of promising topologies, such as a recently predicted amorphous monolayer [25].

From our DFT results, the calculations within a lower-strained supercell result in lower chemical potentials. Thermodynamically metastable intercalated plumbene-like monolayers can be obtained with higher chemical potentials within a higher-strained smaller supercell (6×6)G/(3×3)Si, (4×4)G/(2×2)Si, or (2×2)G/(1×1)Si, relative to plentiful amorphous-like or Pb(111)-like monolayers especially within a low-strained large supercell (13×13)G/(6×6)Si or (26×26)G/(12×12)Si. Relative to the structures under the high-strained buffer-layer graphene, a metastable plumbene-like monolayer with distorted lattice and significantly lower chemical potential can be obtained within a (13×13)G/(6×6)Si supercell. These results should be compared with and are compatible with the recently reported formation of plumbene [13], but additional studies for this important intercalated 2D material system are needed both theoretically and experimentally.

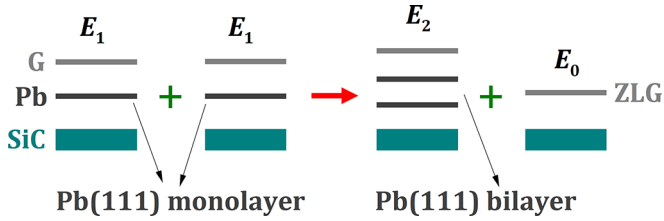


FIG. 10. Schematic for analyzing interlayer interactions of intercalated Pb(111) monolayer and bilayer under decoupled graphene (G) from buffer layer graphene (ZLG) on Si-terminated SiC(0001).

ACKNOWLEDGMENTS

Y.H., M.K., and M.C.T. were supported by the Materials Sciences and Engineering Division, and J.W.E. by the Chemical Sciences, Geosciences, and Biological Sciences Division, of the U.S. Department of Energy (DOE), Office of Science, Basic Energy Sciences. The research was performed at the Ames National Laboratory, which is operated for the U.S. DOE by Iowa State University under Contract No. DE-AC02-07CH11358. This research used resources of the National Energy Research Scientific Computing Center (NERSC), a DOE Office of Science User Facility using NERSC award BES-ERCAP0027660.

APPENDIX A: LATTICE MISMATCHES AND STRAINS IN GRAPHENE, Pb(111), AND PLUMBENE RELATIVE TO SiC(0001)

In our model for calculating the systems of graphene (or ZLG) on Si-terminated SiC(0001) with (or without) Pb intercalated, we always fix the equilibrium lattice constant a_{SiC} of the SiC(0001) substrate, where we take a_{SiC} to be our DFT value 3.09545 \AA [51], despite the fact that there are two (graphene-Pb and Pb-STL) interfaces that can induce strain after a Pb layer is intercalated. For a rhombic supercell $(m \times m)\text{G}/(n \times n)\text{Si}$ without intercalated Pb, the corresponding ZLG-SiC lattice mismatch with a lateral strain ε_{G} is defined by Eq. (1). For seven types of supercells specified by m and n , the corresponding ε_{G} values by taking the freestanding graphene lattice constant $a_{\text{G}} = 2.464 \text{ \AA}$ [50] are listed in column 2 in Table I.

For an intercalated $l \times l$ Pb layer, which can be a single-atom-thick Pb(111) layer [Pb(111) monolayer], a Pb(111) bilayer, or a plumbene monolayer, the corresponding Pb-SiC lattice mismatch with a lateral strain ε_{Pb} is defined by Eq. (2). For seven types of supercells specified by m and n , the corresponding ε_{Pb} values with l specified are listed in columns 4 to 7 in Table I, by taking $a_0 = 3.290 \text{ \AA}$ for a Pb(111) monolayer, 3.290 \AA for a Pb(111) bilayer, 3.546 \AA for a bulk Pb(111) slab, and 4.904 \AA for plumbene (see Sec. III), respectively.

APPENDIX B: DFT DATA FOR CALCULATED CONFIGURATIONS

In Table S1, we list our DFT data (including chemical potentials μ and μ^* with the Pb coverage $\theta = P/N$, and the magnetic moment M) of 104 configurations fully relaxed by using seven types of rhombic supercells $(m \times m)\text{G}/(n \times n)\text{Si}$. A brief description for each configuration is listed in column 8 of Table S1. Given an initial configuration, the fully relaxed states can have different M , and in this case, we always choose a magnetic state with the lowest energy for calculating the corresponding μ and μ^* .

APPENDIX C: AN ILLUSTRATION FOR INTERLAYER INTERACTIONS OF INTERCALATED Pb(111) MONOLAYER AND BILAYER UNDER BUFFER LAYER GRAPHENE ON Si-TERMINATED SiC(0001)

As an example to understand interlayer interactions of intercalated Pb(111) monolayer and bilayer under buffer layer graphene on Si-terminated SiC(0001), a qualitative analysis for energy decomposition is illustrated in Fig. 10. We consider two identical systems (as the reactants) with the total energy E_1 for each, and a Pb(111) monolayer is intercalated in each system (see the left of the red arrow in Fig. 10). Then, we consider two systems (the products) with total energies E_2 and E_0 : one has an intercalated Pb(111) bilayer and one is the pristine ZLG plus Si-terminated SiC(0001) (see the right of the red arrow in Fig. 10). If the energy difference $\Delta E = 2E_1 - (E_2 + E_0) > 0$, then the intercalated Pb(111) bilayer is thermodynamically preferred relative to the intercalated Pb(111) monolayer. If $\Delta E < 0$, then the intercalated Pb(111) monolayer is thermodynamically preferred relative to the intercalated Pb(111) bilayer.

If one mainly considers the nearest-neighbor interlayer interactions, i.e., ignores the contributions from relaxation, longer-range interlayer interactions, etc., the above energy difference can be approximated as $\Delta E \approx \Phi_{\text{PbG}} + \Phi_{\text{PbSiC}} - (\Phi_{\text{PbPb}} + \Phi_{\text{GSiC}})$ after the cancellation of energy terms, where Φ_{PbG} is the interaction between a Pb(111) monolayer and graphene, Φ_{PbSiC} is the interaction between a Pb(111) monolayer and Si-terminated SiC(0001), Φ_{PbPb} is the interaction between two Pb(111) monolayers in a Pb(111) bilayer, and Φ_{GSiC} is the interaction between ZLG and Si-terminated SiC(0001). Here, Φ_{PbPb} should be comparable to the cleavage energy [50] along a Pb(111) plane of a bulk Pb(111) slab, while Φ_{GSiC} is the exfoliation energy [50] of ZLG on Si-terminated SiC(0001). From the DFT results in Sec. IV E, the intercalated Pb(111) monolayer is significantly favored over the intercalated Pb(111) bilayer. This implies that $\Delta E < 0$, and then $\Phi_{\text{PbG}} + \Phi_{\text{PbSiC}} < \Phi_{\text{PbPb}} + \Phi_{\text{GSiC}}$.

[1] J. Wan, S. D. Lacey, J. Dai, W. Bao, M. S. Fuhrer, and L. Hu, Tuning two-dimensional nanomaterials by intercalation: Materials, properties and applications, *Chem. Soc. Rev.* **45**, 6742 (2016).

[2] L. Daukiya, M. N. Nair, M. Cranney, F. Vonau, S. Hajjar-Garreau, D. Aubel, and L. Simon, Functionalization of 2D materials by intercalation, *Prog. Surf. Sci.* **94**, 1 (2019).

- [3] M. S. Stark, K. L. Kuntz, S. J. Martens, and S. C. Warren, Intercalation of layered materials from bulk to 2D, *Adv. Mater.* **31**, 1808213 (2019).
- [4] N. Briggs, Z. M. Gebeyehu, A. Vera, T. Zhao, K. Wang, A. D. L. F. Duran, B. Bersch, T. Bowen, K. L. Knappenberger, and J. A. Robinson, Epitaxial graphene/silicon carbide intercalation: A minireview on graphene modulation and unique 2D materials, *Nanoscale* **11**, 15440 (2019).
- [5] X. Zhao, P. Song, C. Wang, A. C. Riis-Jensen, W. Fu, Y. Deng, D. Wan, L. Kang, S. Ning, J. Dan, T. Venkatesan, Z. Liu, W. Zhou, K. S. Thygesen, X. Luo, S. J. Pennycook, and K. P. Loh, Engineering covalently bonded 2D layered materials by self-intercalation, *Nature (London)* **581**, 171 (2020).
- [6] E. Mazaleyrat, S. Vlačić, A. Artaud, L. Magaud, T. Vincent, A. C. Gómez-Herrero, S. Lisi, P. Singh, N. Bendiab, V. Guisset, P. David, S. Pons, D. Roditchev, C. Chapelier, and J. Coraux, How to induce superconductivity in epitaxial graphene via remote proximity effect through an intercalated gold layer, *2D Mater.* **8**, 015002 (2020).
- [7] A. Yurtsever, J. Onoda, T. Iimori, K. Niki, T. Miyamachi, M. Abe, S. Mizuno, S. Tanaka, F. Komori, and Y. Sugimoto, Effects of Pb intercalation on the structural and electronic properties of epitaxial graphene on SiC, *Small* **12**, 3956 (2016).
- [8] S. Chen, P. A. Thiel, E. Conrad, and M. C. Tringides, Growth and stability of Pb intercalated phases under graphene on SiC, *Phys. Rev. Mater.* **4**, 124005 (2020).
- [9] T. Hu, D. Yang, H. Gao, Y. Li, X. Liu, K. Xu, Q. Xia, and F. Ma, Atomic structure and electronic properties of the intercalated Pb atoms underneath a graphene layer, *Carbon* **179**, 151 (2021).
- [10] D. Yang, Q. Xia, H. Gao, S. Dong, G. Zhao, Y. Zeng, F. Ma, and T. Hu, Fabrication and mechanism of Pb-intercalated graphene on SiC, *Appl. Surf. Sci.* **569**, 151012 (2021).
- [11] M. Gruschwitz, C. Ghosal, T.-H. Shen, S. Wolff, T. Seyller, and C. Tegenkamp, Surface transport properties of Pb-intercalated graphene, *Materials* **14**, 7706 (2021).
- [12] B. Matta, P. Rosenzweig, O. Bolkenbaas, K. Küster, and U. Starke, Momentum microscopy of Pb-intercalated graphene on SiC: Charge neutrality and electronic structure of interfacial Pb, *Phys. Rev. Res.* **4**, 023250 (2022).
- [13] C. Ghosal, M. Gruschwitz, J. Koch, S. Gemming, and C. Tegenkamp, Proximity-induced gap opening by twisted plumbene in epitaxial graphene, *Phys. Rev. Lett.* **129**, 116802 (2022).
- [14] A. Vera, W. Yanez, K. Yang, B. Zheng, C. Dong, Y. Wang, T. Bowen, H. El-Sherif, G. Krishnan, S. Rajabpour, M. Wetherington, R. J. Koch, E. Rotenberg, N. Bassim, V. H. Crespi, C. Liu, N. Samarth, and J. A. Robinson, Emergent spin phenomena in air-stable, atomically thin lead, [arXiv:2205.06859](https://arxiv.org/abs/2205.06859).
- [15] P. Schädlich, C. Ghosal, M. Stettner, B. Matta, S. Wolff, F. Schölzel, P. Richter, M. Hutter, A. Haags, S. Wenzel, Z. Mamiyev, J. Koch, S. Soubatch, P. Rosenzweig, C. Polley, F. S. Tautz, C. Kumpf, K. Küster, U. Starke, T. Seyller, F. C. Bocquet, and C. Tegenkamp, Domain boundary formation within an intercalated Pb monolayer featuring charge-neutral epitaxial graphene, *Adv. Mater. Inter.* **10**, 2300471 (2023).
- [16] Y. Han, S. Chen, J. Hall, S. Roberts, M. Kolmer, J. W. Evans, and M. C. Tringides, Degeneracy in intercalated Pb phases under buffer-layer graphene on SiC(0001) and diffuse moiré spots in surface diffraction, *J. Phys. Chem. Lett.* **14**, 7053 (2023).
- [17] J. Wang, M. Kim, L. Chen, K.-M. Ho, M. Tringides, C.-Z. Wang, and S. Wang, Manipulation of electronic property of epitaxial graphene on SiC substrate by Pb intercalation, *Phys. Rev. B* **103**, 085403 (2021).
- [18] T. Zhang, P. Cheng, W.-J. Li, Y.-J. Sun, G. Wang, X.-G. Zhu, K. He, L. Wang, X. Ma, X. Chen, J. Wang, Y. Liu, H.-Q. Lin, J.-F. Jia, and Q.-K. Xue, Superconductivity in one-atomic-layer metal films grown on Si(111), *Nat. Phys.* **6**, 104 (2010).
- [19] C. Brun, T. Cren, and D. Roditchev, Review of 2D superconductivity: The ultimate case of epitaxial monolayers, *Supercond. Sci. Technol.* **30**, 013003 (2017).
- [20] J. H. Dil, F. Meier, J. Lobo-Checa, L. Patthey, G. Bihlmayer, and J. Osterwalder, Rashba-type spin-orbit splitting of quantum well states in ultrathin Pb films, *Phys. Rev. Lett.* **101**, 266802 (2008).
- [21] K. Yaji, Y. Ohtsubo, S. Hatta, H. Okuyama, K. Miyamoto, T. Okuda, A. Kimura, H. Namatame, M. Taniguchi, and T. Aruga, Large Rashba spin splitting of a metallic surface-state band on a semiconductor surface, *Nat. Commun.* **1**, 17 (2010).
- [22] K. Yang, Y. Wang, and C.-X. Liu, Momentum-space spin antivortex and spin transport in monolayer Pb, *Phys. Rev. Lett.* **128**, 166601 (2022).
- [23] M. Hupalo, X. Liu, C. Wang, W. Lu, Y. Yao, K. Ho, and M. C. Tringides, Metal nanostructure formation on graphene: Weak versus strong bonding, *Adv. Mater.* **23**, 2082 (2011).
- [24] Y. Han, M. Kolmer, M. C. Tringides, and J. W. Evans, Thermodynamics and kinetics of Pb intercalation under graphene on SiC(0001), *Carbon* **205**, 336 (2023).
- [25] C. Wang, T. Cheng, Z. Liu, F. Liu, and H. Huang, Structural amorphization-induced topological order, *Phys. Rev. Lett.* **128**, 056401 (2022).
- [26] W.-F. Tsai, C.-Y. Huang, T.-R. Chang, H. Lin, H.-T. Jeng, and A. Bansil, Gated silicene as a tunable source of nearly 100% spin-polarized electrons, *Nat. Commun.* **4**, 1500 (2013).
- [27] P. Rivero, J.-A. Yan, V. M. García-Suárez, J. Ferrer, and S. Barraza-Lopez, Stability and properties of high-buckled two-dimensional tin and lead, *Phys. Rev. B* **90**, 241408(R) (2014).
- [28] Z.-Q. Huang, C.-H. Hsu, F.-C. Chuang, Y.-T. Liu, H. Lin, W.-S. Su, V. Ozolins, and A. Bansil, Strain driven topological phase transitions in atomically thin films of group IV and V elements in the honeycomb structures, *New J. Phys.* **16**, 105018 (2014).
- [29] T. P. Kaloni, M. Modarresi, M. Tahir, M. R. Roknabadi, G. Schreckenbach, and M. S. Freund, Electrically engineered band gap in two-dimensional Ge, Sn, and Pb: A first-principles and tight-binding approach, *J. Phys. Chem. C* **119**, 11896 (2015).
- [30] H. Zhao, C. Zhang, W. Ji, R. Zhang, S. Li, S. Yan, B. Zhang, P. Li, and P. Wang, Unexpected giant-gap quantum spin Hall insulator in chemically decorated plumbene monolayer, *Sci. Rep.* **6**, 20152 (2016).
- [31] X.-L. Yu, L. Huang, and J. Wu, From a normal insulator to a topological insulator in plumbene, *Phys. Rev. B* **95**, 125113 (2017).
- [32] X.-L. Yu and J. Wu, Evolution of the topological properties of two-dimensional group IVA materials and device design, *Phys. Chem. Chem. Phys.* **20**, 2296 (2018).

- [33] D. K. Das, J. Sarkar, and S. K. Singh, Effect of sample size, temperature and strain velocity on mechanical properties of plumbene by tensile loading along longitudinal direction: A molecular dynamics study, *Comput. Mater. Sci.* **151**, 196 (2018).
- [34] L. Zhang, H. Zhao, W. Ji, C. Zhang, P. Li, and P. Wang, Discovery of a new quantum spin Hall phase in bilayer plumbene, *Chem. Phys. Lett.* **712**, 78 (2018).
- [35] J. Yuhara, B. He, N. Matsunami, M. Nakatake, and G. L. Lay, Graphene's latest cousin: Plumbene epitaxial growth on a "nano watercube" *Adv. Mater.* **31**, 1901017 (2019).
- [36] Y. Li, J. Zhang, B. Zhao, Y. Xue, and Z. Yang, Constructive coupling effect of topological states and topological phase transitions in plumbene, *Phys. Rev. B* **99**, 195402 (2019).
- [37] G. Bihlmayer, J. Sassmannshausen, A. Kubetzka, S. Blügel, K. von Bergmann, and R. Wiesendanger, Plumbene on a magnetic substrate: A combined scanning tunneling microscopy and density functional theory study, *Phys. Rev. Lett.* **124**, 126401 (2020).
- [38] A. Zhao and B. Wang, Two-dimensional graphene-like Xenos as potential topological materials, *APL Mater.* **8**, 030701 (2020).
- [39] N. Katoch, P. Jamdagni, P. K. Ahluwalia, and J. Kumar, Optical properties of mono and bilayer plumbene: A DFT study, *AIP Conf. Proc.* **2265**, 030704 (2020).
- [40] J. Yuhara and G. L. Lay, Beyond silicene: Synthesis of germanene, stanene and plumbene, *Jpn. J. Appl. Phys.* **59**, SN0801 (2020).
- [41] S. Mahdaviifar, S. F. shayesteh, and M. B. Tagani, Electronic and mechanical properties of Plumbene monolayer: A first-principle study, *Physica E* **134**, 114837 (2021).
- [42] Vivek, M. Sharma, and R. Sharma, Plumbene: A next generation hydrogen storage medium, *Int. J. Hydrog. Energy* **46**, 33197 (2021).
- [43] See Supplemental Material at <http://link.aps.org/supplemental/10.1103/PhysRevMaterials.8.044002> for DFT data of 104 configurations fully relaxed by using seven types of rhombic supercells and selected configurations discussed in the text.
- [44] G. Kresse and J. Furthmüller, Efficient iterative schemes for ab initio total-energy calculations using a plane-wave basis set, *Phys. Rev. B* **54**, 11169 (1996).
- [45] G. Kresse and D. Joubert, From ultrasoft pseudopotentials to the projector augmented-wave method, *Phys. Rev. B* **59**, 1758 (1999).
- [46] J. Klimeš, D. R. Bowler, and A. Michaelides, Chemical accuracy for the van der Waals density functional, *J. Phys.: Condens. Matter* **22**, 022201 (2010).
- [47] I. Forbeaux, J.-M. Themlin, and J.-M. Debever, Heteroepitaxial graphite on 6H-SiC(0001): Interface formation through conduction-band electronic structure, *Phys. Rev. B* **58**, 16396 (1998).
- [48] T. Ohta, A. Bostwick, T. Seyller, K. Horn, and E. Rotenberg, Controlling the electronic structure of bilayer graphene, *Science* **313**, 951 (2006).
- [49] J. Hass, W. A. de Heer, and E. H. Conrad, The growth and morphology of epitaxial multilayer graphene, *J. Phys.: Condens. Matter* **20**, 323202 (2008).
- [50] Y. Han, K. C. Lai, A. Lii-Rosales, M. C. Tringides, J. W. Evans, and P. A. Thiel, Surface energies, adhesion energies, and exfoliation energies relevant to copper-graphene and copper-graphite systems, *Surf. Sci.* **685**, 48 (2019).
- [51] Y. Han, J. W. Evans, and M. C. Tringides, Dy adsorption on and intercalation under graphene on 6H-SiC(0001) surface from first-principles calculations, *Phys. Rev. Mater.* **5**, 074004 (2021).
- [52] Y. Han, J. W. Evans, and M. C. Tringides, Energy barriers for Dy and H penetrating graphene on 6H-SiC(0001) and freestanding bilayer graphene from first-principles calculations, *Appl. Phys. Lett.* **119**, 033101 (2021).
- [53] M. E. Straumanis, The precision determination of lattice constants by the powder and rotating crystal methods and applications, *J. Appl. Phys.* **20**, 726 (1949).
- [54] W. Joss, Fermi surface of lead under homogeneous strain, *Phys. Rev. B* **23**, 4913 (1981).
- [55] L. Brewer, The cohesive energies of the elements, Report No. LBL-3720 Rev (Lawrence Berkeley National Laboratory, University of California, Berkeley, 1977), <https://escholarship.org/uc/item/08p2578m>.
- [56] K. A. Gschneidner, Physical properties and interrelationships of metallic and semimetallic elements, *Solid State Phys.* **16**, 275 (1964).
- [57] S. Cahangirov, M. Topsakal, E. Aktürk, H. Şahin, and S. Ciraci, Two- and one-dimensional honeycomb structures of silicon and germanium, *Phys. Rev. Lett.* **102**, 236804 (2009).
- [58] W. Li, L. Huang, R. G. S. Pala, G.-H. Lu, F. Liu, J. W. Evans, and Y. Han, Thickness-dependent energetics for Pb adatoms on low-index Pb nanofilm surfaces: First-principles calculations, *Phys. Rev. B* **96**, 205409 (2017).
- [59] W. Li, L. Huang, M. C. Tringides, J. W. Evans, and Y. Han, Thermodynamic preference for atom adsorption versus intercalation into multilayer graphene, *J. Phys. Chem. Lett.* **11**, 9725 (2020).
- [60] S. Chen, Y. Han, M. Kolmer, J. Hall, M. Hupalo, J. W. Evans, and M. C. Tringides, Targeted Dy intercalation under graphene/SiC for tuning its electronic band structure, *Phys. Rev. B* **107**, 045408 (2023).